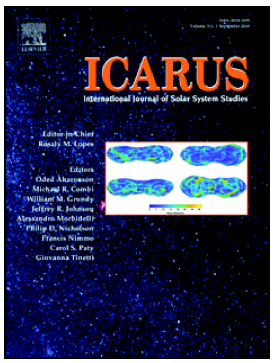

Spectral reflectance properties of nontronite exposed to Mars-like surface conditions and low-temperature heating (<300 °C)

Nathalie Turenne, Sahejpal Sidhu, Daniel M. Applin, Edward A. Cloutis, Z.U. Wolf, Stanley A. Mertzman, Elisabeth M. Hausrath, Teresa Fornaro, Adrian Brown

PII: S0019-1035(23)00025-8

DOI: https://doi.org/10.1016/j.icarus.2023.115448

Reference: YICAR 115448

To appear in: *Icarus*

Received date: 12 July 2022

Revised date: 24 January 2023

Accepted date: 25 January 2023

Please cite this article as: N. Turenne, S. Sidhu, D.M. Applin, et al., Spectral reflectance properties of nontronite exposed to Mars-like surface conditions and low-temperature heating (<300 °C), *Icarus* (2023), https://doi.org/10.1016/j.icarus.2023.115448

Spectral reflectance properties of nontronite exposed to Mars-like surface conditions and low-temperature heating (<300°C)

Nathalie Turenne[1], Sahejpal Sidhu[1], Daniel M. Applin[1], Edward A. Cloutis[1], Z. U. Wolf[1] Stanley A. Mertzman[2], Elisabeth M. Hausrath[3], Teresa Fornaro[4] and Adrian Brown[5]

[1] Centre for Terrestrial and Planetary Exploration, University of Winnipeg, Winnipeg, Manitoba R3B 2E9, Canada

[2] Department of Earth and Environment, Franklin and Marshall College, P.O. Box 3003, Lancaster, PA, 17604-3003 USA.

[3] Department of Geoscience, University of Nevada, Las Vegas, Las Vegas, Nevada, 89154, USA.

[4]INAF-Astrophysical Observatory of Arcetri, Largo E. Fermi 5, 50125 Florence, Italy.

[5]Plancius Research, Severna Park, MD 21146.

Corresponding author: Nathalie Turenne
Centre for Terrestrial and Planetary Exploration
University of Winnipeg
515 Portage Avenue
Winnipeg, Manitoba, Canada R3B 2E9
Tel: 204 786 9326
E-mail: turenne-n@webmail.uwinnipeg.ca

Abstract: Spectral reflectance properties of nontronite [a phyllosilicate with an ideal formula of $Na_{0.3}Fe_2^{3+}(Si,Al)_4O_{10}(OH)_2 \cdot nH_2O$] were investigated under simulated Mars surface conditions of atmospheric pressure and composition, and after heating to 110°, 180°, and 300° C. The data can be used to determine the conditions to which nontronites on the martian surface may have been subjected. Nontronite's spectral features include Fe^{3+} associated absorption features below 1000 nm, H_2O/OH features near 1400 nm, H_2O features near 1900 nm, a characteristic metal-OH (Fe^{3+}) feature in the 2280-2290 nm region, and an additional Fe-OH absorption feature near 2400 nm. Heating in a low-pressure CO_2 environment leads to the loss of Fe-OH-associated features below 1000 nm at temperatures as low as 110°C. Both OH and H_2O are progressively lost upon heating to 300°C, but small, spectrally-detectable amounts remain at 300°C. The longer wavelength Fe-OH absorption bands in the 2280 and 2400 nm region persist up to these temperatures. Comparison to other smectites and Fe-rich phyllosilicates show that a strong 2280-2290 nm absorption feature and weak or absent ~2320 nm feature are unique to nontronite. A broader absorption feature in the 2300 nm region suggests the presence of nontronite and one or more Mg-bearing phyllosilicate(s). A Mg^+Fe^{3+} phyllosilicate is implausible because of the difficulty in incorporating Mg^{2+} into the dioctahedral structure of nontronite. With increasing grain size, nontronite spectra become darker and progressively more blue-sloped beyond ~1500 nm with absorption bands showing increasing depth until saturation is reached for some of them beyond a few hundred-micron grain size. The spectral changes documented in this study, as well as a comparison to previous studies, suggest that the absorption features associated with nontronite can be used to place constraints on conditions that nontronite may have been exposed to in the past. This study demonstrates that dehydration as well as dehydroxylation can occur at temperatures <300°C.

Keywords: Mars, Nontronite, Mineralogy, Phyllosilicates, Spectroscopy**,** Search for Extraterrestrial Life

1. Introduction

Detection of phyllosilicate minerals on Mars dates to at least the 1980s based on various diagnostic absorption features seen in Earth-based telescopic spectra (e.g., Singer, 1982); however, the nature of the phyllosilicates could not be confidently determined at the time. More recently, spectral signatures indicative of phyllosilicates have been observed by the Compact Reconnaissance Imaging Spectrometer for Mars (CRISM) onboard the Mars Reconnaissance orbiter and the Observatoire pour la Mineralogie, L'Eau, les Glaces et l'Activite (OMEGA) spectrometer on the Mars Express orbiter (Poulet et al., 2005; Bibring et al., 2006; Mustard et al., 2008; Ehlmann et al., 2009, 2011; Brown et al., 2010; Murchie et al., 2009). These detections are based largely on absorption features in the 2000-2500 nm region. Most phyllosilicate occurrences detected on Mars are associated with ancient and heavily-cratered terrains (Che and Glotch, 2012). A proportion of these deposits were likely repeatedly subjected to impact-generated heating and such thermally-altered phyllosilicates could be present on the surface of Mars today (Che and Glotch, 2012; Gavin and Chevrier, 2010).

Fe-Mg smectites, which can include nontronite [ideal formula: $Na_{0.3}Fe_2^{3+}(Si,Al)_4O_{10}(OH)_2 \cdot nH_2O$], have been detected in multiple locations on the martian surface, including Mawrth Vallis, Nili Fossae, Terra Meridiani, Gale Crater, and north of the Syrtis Major volcanic plateau (Bibring et al., 2005; Poulet et al., 2005, 2007; Bibring et al., 2006; Michalski and Noe Dobrea, 2007; Clark et al., 2007; Ehlmann et al., 2008, 2009; Mustard et al., 2008; Murchie et al., 2009; Wray et al., 2009; Milliken et al., 2010; Ehlmann and Mustard, 2012; Carter et al., 2013). The detection of phyllosilicates on Mars is largely based on the presence of hydration bands at ~1400 nm, and metal-OH vibrational bands at ~2200 nm (Al-OH), ~2290 nm (Fe-OH), and >~2320 nm (Mg-OH) (Poulet et al., 2005). The 2280-2290 nm absorption feature has been interpreted as being attributable to Fe-bearing smectites, which can include nontronite.

Some of the current Mars landed missions are located in regions where phyllosilicates are present based on orbital and in situ data. Fe-rich phyllosilicates have been documented within the sediment deposits in Gale Crater (Milliken et al., 2009, 2010) the landing site of the Curiosity Rover, in the region of Jezero Crater (Schon et al., 2012; Salvatore et al., 2018; Wiens et al., 2022), the landing site of the NASA Mars 2020 Perseverance Rover, and at Oxia Planum (found

between Ares Vallis and Mawrth Vallis), the landing site for the future ESA ExoMars Rosalind Franklin rover mission (Quantin et al., 2016; Ivanova et al., 2020). A more detailed account of several nontronite identifications is presented in section 1.1.

This study builds on previous studies of the stability and spectroscopic properties of the Fe-smectite phyllosilicate nontronite and the spectroscopic basis of its detectability on the surface of Mars. We focused on exposing nontronite to Mars-like surface conditions of atmospheric pressure and composition, and progressively heated the samples to temperatures up to 300°C. This complements several previous studies which were conducted under different conditions and/or over different temperature intervals or periods of heating (e.g., Boslough et al., 1980; Weldon et al., 1982; Cloutis et al., 2007; Gavin and Chevrier, 2010; Morris et al., 2010; Che and Glotch, 2012; Gavin et al., 2013; Friedlander et al., 2015; Michalski et al., 2017). We also spectrally characterized a suite of 5 nontronite samples to assess any spectral variability of natural samples and assessed whether grain size variations can mimic spectral variations associated with low-pressure CO_2 environments and heating. The goals of the study were to a) determine nontronite's unique UV-VIS-NIR spectral properties for orbital and in situ spectral detections, b) determine how nontronite reflectance spectra vary when this mineral is exposed to different conditions (in particular low-level (<300°C) heating in a low-pressure CO_2 atmosphere), and c) determine what spectral properties of nontronite could be used to constrain conditions to which nontronite has been exposed. We focused on heating below 300°C because this has been a largely unexplored temperature range, and has not been previously examined in a low-pressure CO_2 environment. Temperatures below ~350°C are associated largely with dehydration while higher temperatures are associated with dehydroxylation (Ding and Frost, 2002). This study fills an important gap in understanding the spectroscopic properties of nontronite as they relate to Mars. Low-temperature heating (below the dehydroxylation temperature) could arise from a number of causes, such as heating due to an impact event, burial under impact ejecta, ashfall, and/or lava flows.

1.1. Detection of Fe/Mg-smectites on Mars

Fe/Mg smectites have been detected in a number of regions on Mars and have been based largely on the presence of absorption features in the ~2280 and ~2320 nm regions. Some of these detections and the basis for the detections are summarized below.

1.1.1 Mawrth Vallis region

Fe/Mg-bearing phyllosilicates were detected in the Mawrth Vallis outflow channel using the OMEGA spectrometer on board the Mars Express orbiter (Poulet et al., 2005, Loizeau et al., 2007). The detection of Fe-bearing smectites was mainly based on the hydration bands seen at 1410 and 1930 nm, in addition to the metal-OH vibrational bands at ~2290 nm (Fe-OH), and >2320 nm (Mg-OH) (Loizeau et al., 2007; Poulet et al., 2005). Data from CRISM showed absorption features at ~1400, 1920, 2300, and 2390 nm that were attributed to the presence of Fe/Mg phyllosilicates in the western region of Mawrth Vallis (Bishop et al., 2008a). Origins of the clay-rich region found at Mawrth Vallis were proposed to be either from the deposition of non-hydrated minerals that were subsequently altered by groundwater activity or weathering, or alteration that occurred elsewhere, and the post-alteration sediments were deposited into the Mawrth Vallis region (Loizeau et al., 2010). Modeling of the distribution of these minerals has helped to shed light on past aqueous conditions in this area (Gainey et al., 2022).

1.1.2 Oxia Planum region

Oxia Planum is the planned landing site of the ESA Rosalind Franklin rover. It is located between two major outflow channels: Ares Vallis and Mawrth Vallis. CRISM data identified a range of absorption bands within Oxia Planum and its catchment area related to phyllosilicates (Brossier et al., 2022). These observations are consistent with spectral interpretations made in the immediate region around Mawrth Vallis (Bishop et al., 2008a). Oxia Planum's phyllosilicate spectra are consistent with the presence of Fe/Mg-rich phyllosilicates (nontronite and saponite) mixtures (Brossier et al., 2022) Spectra of outcrops within the catchment area are consistent with those of nontronite, based on the narrow absorption band at 2290 nm in addition to the 1410, 1920, and 2400 nm absorption features (Brossier et al., 2022; Noe Dobrea, 2010).

1.1.3 Gale crater region

Nontronites and other clay minerals in Gale crater were detected from analysis of CRISM data based on absorption features at ~1400, ~1900, and ~2290 nm (Milliken et al., 2009, 2010). Gale crater has been interpreted to have hosted sediment deposition and erosion as seen by the horizontal depositional patterns of the lower, exposed strata (Malin and Edgett, 2000; Milliken et al., 2010). The central mound in Gale crater, termed Mt. Sharp, is divided into two major

formations: the upper and the lower. Fe-smectites that match with laboratory spectra of nontronites are found in the thin beds below the lower-middle member contact formation (Milliken et al., 2010). Sulfates overlie the clay minerals in the lower formation, suggesting that a change occurred from a clay-conducive environment to a sulfate-conducive environment (Bibring et al., 2006; Milliken et al., 2010).

1.1.4 Jezero Crater region

Jezero Crater lies south of the Nilli Fossae region and is host to several outcrops of Fe/Mg smectites as determined from analysis of OMEGA data (Ehlmann et al., 2008; Poulet et al., 2005) and CRISM (Ehlmann et al., 2008; Mustard et al., 2008; Goudge, et al. 2015). Clay-rich sediments from the Noachian plateau were transported to Jezero Crater through drainage valleys (Ehlmann et al., 2008; Poulet et al., 2005). Absorption features near 1900 and 2300 nm were used to identify smectites (Ehlmann et al., 2008). The 2300 nm band position suggests a phyllosilicate that is intermediate between nontronite (band position: ~2285 nm) and saponite (band position: ~2315 nm) (Ehlmann et al., 2008). Smectite-forming fluids were likely moderate to alkaline pH during their deposition (Ehlmann et al., 2008). Recent in-situ detections using the SuperCam VISIR spectrometer have determined that iron-rich phyllosilicates such as nontronite and hisingerite are abundant in Jezero crater's Máaz formation. The detections are based on the 2280 nm absorption band which is frequently paired with the 1420 and 1920 nm hydration bands, along with a 2400 nm absorption band (Wiens et al., 2022). Wiens et al., (2022) suggest some chemical weathering occurred in Jezero crater due to the presence of alteration products in the IR spectra such as Fe-rich phyllosilicates.

1.1.5 Syrtis Major region

Northeast of Syrtis Major, four stratigraphic layers occur, with the lowermost layer consisting of Fe/Mg smectites and pyroxene (Ehlmann and Mustard, 2012). The basement layer consisted of low-calcium pyroxene that experienced at least partial aqueous alteration to produce Fe/Mg smectites (Ehlmann et al., 2009; Ehlmann and Mustard, 2012). However, this lowest stratigraphic layer forms the highest topographical hills within the region, with the Mg smectites being identified by 1390 and 2310 nm absorption bands seen in CRISM data (Ehlmann and Mustard, 2012). An olivine-rich unit sits atop the basement Fe/Mg smectite-pyroxene layer

which was likely deposited from lava flows subsequent to the Isidis Basin impact (Brown et al. 2020).

1.1.6 Terra Meridiani region

Terra Meridiani is a region near the Arabia Terra where the presence of hydrated minerals has been observed, as seen by the hydration band at ~1900 nm in OMEGA data (Poulet et al., 2007). Small amounts of phyllosilicates have also been detected within northern Terra Meridiani and Arabia Terra in eroded outcrops suggesting a history of aqueous alteration (Poulet et al., 2005). However, these detections are found mixed with sulfate deposits (Poulet et al., 2005). Absorption features around 1900 and ~2300 ± 100 nm were used to identify and map Fe/Mg-bearing smectites (Poulet et al., 2005).

2. Nontronite's crystal structure and spectroscopic properties

2.1 Crystal structure

Smectite clays are layer-lattice phyllosilicates with exchangeable interlayer cations and the ability to incorporate and retain interlayer water (Odom, 1984). The smectite structure consists of one octahedral sheet sandwiched between two inward-facing tetrahedral sheets; hence it is termed a 2:1 phyllosilicate (Odom, 1984). Between adjacent tetrahedral-octahedral-tetrahedral (T-O-T) layers, water and other cations are present. If isomorphic substitution of cations with lower valence occurs in the crystal lattice of phyllosilicates, a permanent negative charge arises and requires exchangeable cations in the interlayer space to balance the overall charge. This gives a swelling capacity to smectite clays as the exchangeable cations attract and bond to water and can thus be in various hydration states. Depending on the cations present in the interlayers, a smectite clay may undergo swelling post-hydration as layer spacing increases with increasing amounts of interlayer water (Odom, 1984). Interlayer spacing is between ~10 to 15 Å (Varma, 2002), however, it can increase by several Å as reactions take place in the interlayer (Adams et al., 1983).

Nontronites are iron-rich smectite clay with a 2:1 phyllosilicate structure. The tetrahedral layer consists of (Si^{4+}, Al^{3+}, Fe^{3+})O tetrahedra, while the octahedral layer contains Fe^{3+}, as well as Na and other cations (Merola et al., 2007; Palchik et al., 2013). The most probable cation combinations in nontronites are [4Si]($3Fe^{3+}$) and [$1Al_3Si$]($3Fe^{3+}$) (Daynyak and Drits, 1987). It

appears that the substitution of Mg^{2+} into nontronite's dioctahedral structure is extremely limited, and the presence of Mg in "nontronite" is due to the segregation of Mg into trioctahedral domains (Petit et al., 2017 and references therein).

In the octahedral layer, the most common cations that occupy these sites are Fe^{3+}, Al^{3+}, and Mg^{2+}. Fe^{3+} can occur in two configurations, termed *cis* and *trans*. In both sites, Fe^{3+} is bonded to 4 oxygen and 2 OH groups, which differ in the locations of the O and OH groups (Goodman et al., 1976; Bonnin et al., 1985; Bishop et al., 2002; Wang et al., 2020). In dioctahedral smectites, one-third of the octahedral positions are vacant. In nontronites, the *trans* sites are usually unoccupied (Besson et al., 1983). The relative occupancies of the *cis* and *trans* sites by Fe^{3+} have a major impact on the temperature of dehydroxylation (Wang et al., 2020).

2.2 Spectroscopic properties of nontronites (350-2500 nm)

Figure 1 shows the reflectance spectra of several nontronite samples included in this study. The spectra show a number of absorption features that can be assigned to various mechanisms. In general, absorption features below ~1000 nm are attributable to the presence of Fe^{3+} (e.g., Karickhoff and Bailey, 1973; Weldon et al., 1982; Sherman and Vergo, 1988). At the lowest wavelengths, the steep reflectance drop-off below ~500 nm is assigned to intense Fe^{3+}-O charge transfers (Sherman and Vergo, 1988). The narrow feature near 450 nm is attributed to Fe^{3+} "pair excitations", with a possible second absorption feature near 430 nm due to the excitation of Fe^{3+} in tetrahedral coordination (Sherman and Vergo, 1988). An absorption feature in the 670-710 nm region has been assigned to octahedrally coordinated Fe^{3+} ligand field transitions (Bishop et al., 2002a) and/or Fe^{3+}-Fe^{2+} intervalence charge transfers (IVCT) (Sherman and Vergo, 1988). A broad feature in the 900 nm region is assigned to Fe^{3+} ligand field transitions. An absorption feature, usually expressed as a doublet, in the 1400-1450 nm region is assigned to an overtone of the hydroxyl (OH) stretching vibration (e.g., Clark et al., 1990). The complexity of this band is a function of differences in *cis* and *trans* bond lengths (Sherman and Vergo, 1988; Bishop et al., 2002b). An absorption "shoulder" located closer to 1460 nm is likely associated with O-H stretching of interlayer water (Clark et al., 1990; Bishop et al., 1994). The absorption feature near 1900 nm is attributed to nontronite's interlayer water (Clark et al., 1990) and a longer wavelength shoulder near 1970 nm would be attributable to adsorbed water (Bishop et al., 1994). The weak absorption features in the 2200 nm are attributable to Al-OH stretching + bending combinations

and/or quartz Si-OH vibrations (Clark et al., 1990; Rice et al., 2013). The absorption band near 2280 nm is due to an OH stretch plus Fe-OH bend (Clark et al., 1990; Bishop et al., 2002a). A weaker band near 2400 nm has been assigned to a Fe-OH stretch plus bend involving Fe^{3+} in tetrahedral coordination and/or distorted octahedral site (Bishop et al., 2002a, 2002b). The reflectance drops off beyond ~2300 nm is likely attributable to the short wavelength wing of OH and H2O stretching fundamentals in the 2700-3100 nm region as well as a ~2500 nm tetrahedral Fe^{3+}-OH stretching plus bending combination (Clark et al., 1990; Bishop et al., 2002a, 2002b). In summary, nontronite reflectance spectra in the 350-2500 nm region are directly linked to Fe^{3+} in some way, largely via bonding to hydroxyl.

Several factors will affect the reflectance spectra of nontronites and the appearance of absorption bands, such as structural order, cation substitutions, stacking disorders, etc. (e.g., Besson et al., 1983; Bonnin et al., 1985; Bishop et al., 2002a, 2002b; Gates et al., 2002; Wang et al., 2020).

2.3 Nontronite formation conditions

Several formation conditions relevant to nontronite are discussed below, but these are not all conditions that limit the formation of nontronite. Nontronites can form in both terrestrial and marine environments ranging from neutral to alkaline due to weathering of protoliths, as ocean sediments, and hydrothermal deposits as Fe-rich bedrock undergoes hydrothermal alteration (Harder, 1976, 1978; Wilson, 2013; Gainey et al., 2017; Petit et al., 2017). Nontronite formation can also occur as a result of weathering (intermediate stages) of basalts, serpentines, and gabbros (Velde, 2014).

Naturally, nontronites form via the oxidation of trioctahedral Fe (II) silicate into dioctahedral nontronites (Baker and Strawn, 2014; Farmer et al., 1991, 1994). Results from Gainey et al., (2017) indicate that nontronites can form under oxidizing conditions, producing smectites that may retain a low concentration of organics within their structure. Petit et al. (2017) concluded that nontronite synthesis can occur over various temperature ranges (low ambient temperatures to ~200°C) and various redox conditions (Petit et al., 2017). Under authigenic conditions, formation temperatures range from 2-3°C and within hydrothermal deposits ~150°C (Petit et al., 2017; Wilson, 2013).

Nontronites can form from Fe^{2+}-containing solutions after several days under low temperatures (3-20°C) while under anoxic and/or reducing conditions (Harder, 1976, 1978; Chemtob et al., 2017). Additionally, Harder (1978) also concluded that higher pH values and negative Eh (oxidation/reduction potential) values favored the synthesis of Fe-clays like nontronites (Harder, 1978). Such conditions may occur in nature for example in sediment from both freshwater or saltwater, and in bottom water layers (Harder, 1978).

2.4 Nontronite versus hisingerite and other phyllosilicates

Hisingerite has been suggested as possibly being present in Jezero Crater based on a presumed spectral similarity to nontronite (Wiens et al., 2022). Hisingerite (ideal formula: $(Fe^{3+}{}_2Si_2O_5(OH)_4.nH_2O)$) is a hydrous iron silicate that has been suggested as possibly being spectrally similar to nontronite in the VIS-NIR wavelength region (~300-2500 nm) (Milliken et al., 2014). Eggleton and Tilley (1998) determined that hisingerite is conclusively not similar to nontronite structurally; it is a hydrated, ferric, kaolin mineral: an Fe^{3+} analog to kaolinite and halloysite (Milliken et al., 2014; Evans et al., 2017; Tutolo et al., 2019). Hisingerite's chemical properties diverge from nontronite with lower aluminum and a 1:1 octahedral: tetrahedral cation ratio (Eggleton and Tilley, 1998). Hisingerite may be more common on Mars than on Earth due to the higher levels of Fe in the mantle of Mars (Evans et al., 2017; Tutolo et al., 2019).

Hisingerite can form through weathering, deuteric alteration, or hydrothermal alteration (Eggleton and Tilley 1998). Hisingerite can occur in a variety of geological environments but most commonly results as an alteration mineral from pyroxene and olivine-bearing iron gabbroic rocks (Whelan and Goldich, 1961). Hisingerite is known to form in low–temperature environments (~200°C) or through the hydrothermal alteration of ferroan olivine-bearing rocks as a serpentinization product (Evans et al., 2017; Tutolo et al., 2019). Additionally, unlike smectites, hisingerite has a curved or spherical morphology which traps water within those structural spheres but does not hold water in interlayer regions (Eggleton and Tilley 1998). For nontronite formation, the presence of Al-bearing protoliths such as basalt is necessary. At low temperatures, basalts exposed to water will produce clays such as nontronite. The abundance of plagioclase, and its aluminum, will strongly favor the production of an Al-bearing alteration product. Unlike nontronite, hisingerite and serpentine formation require an Al-poor protolith.

The implications for hisingerite versus nontronite spectral detection are discussed in a subsequent section.

2.5 The role of smectites in organic accumulation and synthesis

Clay minerals like smectites tend to accumulate organics due to their large surface area and optimal interlayer sites and favor the preservation of organic molecules because their fine particles aggregate forming small pores that limit penetration of fluids and limiting damaging radiation (Negron-Mendoza and Ramos-Bernal, 2004; Fornaro et al., 2018a, 2018b; Razzell Hollis et al., 2021). By providing shelter and protection against thermal destruction for organics in extreme environments, the interlayer in smectites can act as a place for organic synthesis (Williams et al., 2005). Under experimental conditions simulating hydrothermal seafloor conditions, montmorillonite and saponite (expanding smectites) catalyzed the synthesis of far more organic compounds from methane than illite, a non-expanding smectite (Williams et al., 2005). Adams et al. (1983) found that reactions between 2-methyl pent-2-ene with primary alcohols can occur on the surface and in the interlayer of Al-montmorillonite (Adams et al., 1983). Kennedy et al. (2002) also found that the smectite interlayer can protect against oxidation or metabolization of organic matter. Smectite protection against harsh environments is important for Mars as they not only serve as geochemical markers for past aqueous environments but they serve as reservoirs for hosting organic compounds due to their structure.

Poch et al. (2015) carried out mid-UV irradiation experiments under martian-like temperature and pressure on glycine and adenine molecules co-deposited with nontronite from an aqueous solution. Observation determined a reduction of the efficiencies of photodecomposition of these organic molecules by a factor of 5 in the presence of nontronite, along with additional photoprotection by a factor of 5 from doubling the amount of nontronite in the sample of glycine. These observations strongly suggest that the photoprotection provided by nontronite is not only due to mechanical shielding, but also a sort of stabilizing molecule-mineral interaction takes place, such as electrostatic interactions of the molecules in the interlayers and/or on the edges of nontronite, allowing a more efficient energy dissipation and/or easier recombination for the fragments of the photo-dissociated molecules. Nontronite has been shown to promote an acceleration of the dissociation of urea, maybe due to its greater ability to chelate Fe^{3+} ions with respect to glycine and adenine, which may be responsible for a more efficient photo-oxidation

and decomposition. Dos Santos et al. (2016) also confirmed the photoprotective properties of smectites like montmorillonite, nontronite, and saponite towards amino acids under martian-like UV irradiation conditions.

3. Materials and methods

A total of five nontronite samples were included in this study in addition to three hisingerite samples (two are from the NASA RELAB public spectral database: https://pds-speclib.rsl.wustl.edu/search.aspx) a gibbsite sample (**Table 1**) and a wide variety of other phyllosilicates. The samples were characterized by reflectance spectroscopy (350-2500 nm), compositionally by X-ray fluorescence spectroscopy and wet chemistry (**Table 2**), and structurally by X-ray diffractometry, (**Table 3**).

3.1 Sample preparation

For subsequent analyses, samples were prepared by hand crushing the samples using an alumina mortar and pestle under a fume hood, and dry sieved using stainless steel sieves. Hand crushing minimizes any alteration that may occur from heating using mechanical crushers. Dry sieving involved alternately shaking, gently brushing, and lightly tapping while the sample was in its respective sieve. This was done to avoid any alteration of the sample that may occur with the use of liquid solvents for wet sieving. All samples were crushed and sieved to <45 µm. In addition, grain size fractions of <45, 45-90, 90-106, 106-212, 212-430, and 430-1000 µm were prepared for the NON105 sample.

3.2 Reflectance spectroscopy

An Analytical Spectral Devices (Boulder, CO) Labspec 4 Hi-Res® spectrophotometer was used to collect reflectance spectra from 350 to 2500 nm at a viewing geometry of i=30° and e=0°. An in-house tungsten light source was used to provide incident lighting with a divergence of <1.5° with a fully illuminated spot size of 10 mm. A total of 500 spectra per sample, standard, and dark current were acquired and averaged to improve the signal-to-noise ratio (SNR). The spectrometer collects data with a spatial resolution of between 2 and 7 nm, and a spectral sampling interval of 1.4 nm, which is then internally resampled by the spectrometer to output data at 1 nm intervals. The spectra were corrected for dark current, small absorption features

beyond ~2000 nm in the absolute reflectance of Spectralon, as well as occasional small reflectance offsets at 1000 and 1830 nm, where detector changeovers occur.

An absorption band in the 2280 nm region appears to be uniquely associated with nontronite, as discussed below. The depth of the absorption band near 2280 nm was calculated as follows: a straight-line continuum was constructed that was tangent to the reflectance spectrum on either side of this feature, near 2250 and 2310 nm. The reflectance spectrum was divided by the continuum and the depth was calculated as:

$$1 - \frac{Rb}{Rc}$$

Rb is the reflectance of the continuum-removed spectrum at the position of lowest reflectance, and Rc is the reflectance of the straight-line continuum at the same wavelength position as Rb (Clark and Roush, 1984).

The same procedure was used to determine the depth of the 2320 nm region absorption band. In this case, the straight-line continuum was tangent to the reflectance spectra near 2250 nm and in the ~2360-2420 nm region. Band centers were calculated after isolating the 2280-90 nm absorption band using a straight-line continuum fixed to the reflectance spectrum at 2245 and 2325 nm for each spectrum and finding the wavelength value and reflectance at the point of minimum reflectance between the anchor points using the Excel calculation (=min(2245:2325)). This procedure was conducted on all absorption features listed in **Table 4**. Table 4 also includes band minima which were identified using the same Excel calculation on the original reflectance spectra to determine the wavelength position of the lowest value in the regions of the absorption bands of interest. Band minima may not reflect the true band center due to slope changes, therefore band centers have been used in this study.

3.3 X-ray fluorescence and wet chemistry

Compositional analysis was carried out at Franklin and Marshall College using a Malvern PANalytical, Inc. Zetium X-ray fluorescence (XRF) spectrometer to identify major and selected minor elements and wet chemistry (WC) to determine ferrous iron content. Details of the procedures can be found in Reichen and Fahey (1962), Govindaraju (1994), and Mertzman

(2000), and on-line at: https://www.fandm.edu/earth-environment/laboratory-facilities/xrf-and-xrd-lab. Compositional data are provided in **Table 2**.

3.4 X-ray diffraction (XRD)

XRD characterization of the samples was done using <45 µm powdered subsamples. The XRD analysis involved acquiring continuous scan data from 5 to 80º 2θ on a Bruker D8 Advance with a DaVinci automated powder diffractometer. A Bragg-Brentano goniometer with a two theta/theta setup was equipped with a 2.5° incident Soller slit, a 1.0 mm divergence slit, a 1.0 mm scatter slit, a 0.2 mm receiving slit, a curved secondary graphite monochromator, and a scintillation counter collecting at an increment of 0.02° and integration time of 1 second per step. The line focus Co X-ray tube was operated at 40 kV and 40 mA, using a take-off angle of 6º. Phases identified by XRD analysis are provided in **Table 3**. The X-ray diffractograms are included in the **online supplement**.

3.5 Heating of nontronite under Mars-like surface conditions

The NON101 sample was exposed to several elevated temperatures to replicate impact-induced heating that may occur on Mars, and under Mars-like surface conditions. This experiment was designed to complement previous impact and elevated heating experiments discussed below. The <45 µm sample was put into an 8 mm diameter and 6 mm deep sample cup. The sample was heated using a sealed vacuum oven to 110°C, 180°C, and 300°C for one week each with a continuous flow of CO_2 gas to create atmospheric conditions to simulate those found on early Mars, with pressures between 20 and 100 millibars. This experimental setup was conducted due to the importance to understand the effects of temperature as a separate process from pressure. French (1998) determined that the nonlinear relationship between temperature and pressure in impact environments would make it unlikely that temperatures would exceed 500°C in shocked materials. Reflectance spectra were acquired using an ASD FieldSpec Pro spectrophotometer equipped with a bifurcated cable attached to a 150 W light source. The samples were removed from the vacuum oven for spectral measurements and put back in the vacuum oven for the next temperature interval. Sample spectra were acquired both before and after heating to each temperature, without and through a 10 mm-thick sapphire window after the sample was removed from the oven, allowed to cool to ambient temperature, and briefly exposed to terrestrial ambient conditions. This was done to allow for direct comparison to data from

Cloutis et al. (2007). The spectroscopic data included in this study are provided in the **online supplement**.

4. Results

4.1 Nontronite spectral variability

Nontronites exhibit a number of spectral features attributable to Fe^{3+}, including absorption bands in the ultraviolet-visible wavelength region near 260, 370, 450, 650, and 950 nm. The bands in the 260 and 370 nm region are attributed to Fe-O charge transfers, while the 450, 650, and 950 nm bands are attributed to spin-forbidden transitions in Fe^{3+} (Sherman, 1985; Sherman and Vergo, 1988). The absorption feature present in nontronite spectra near 1400 nm represents the OH stretching overtones of both structural OH and molecular H_2O (Bishop et al., 2008b). OH, will result in a lower wavelength absorption feature than H_2O (Clark et al., 1990). The spectral feature near 1900 nm represents a stretching + bending combination band of molecular H_2O and is most often attributed to interlayer water (Bishop et al., 2008b). The ~2280 and 2400 nm bands represent Fe-OH combination vibrations (Clark et al., 1990; Bishop et al., 2008a, 2008b, 2011, 2013).

The XRD data indicated that all the samples used in this study were dominated by nontronite. This was confirmed by comparing the compositional data to ideal nontronite and further confirmed by XRD analysis. The data did indicate some impurities in the nontronite samples (**Table 3**), while the XRF data (**Table 2**) indicated compositional differences between samples, which could account for the small shifts between (2280-2290) in the position of the 2280 nm feature in the nontronite spectra. The largest compositional differences are for SiO_2, and Fe_2O_3 (**Table 2**). The former can be due to the presence of quartz as indicated by XRD and the latter is likely due to the presence of additional Fe oxyhydroxides, but whose presence was not detected in the XRD spectra (with the exception of NON104 in which a small amount of goethite was detected), perhaps due to their low degree of crystallinity, low abundances, or small grain size. X-ray diffractograms and peak identifications are provided in the **online supplement**.

The NON101-105 spectra all exhibit absorption bands characteristic of Fe^{3+} below 1000 nm. Compositionally, NON104 contains the most Fe_2O_3 wt.% as seen in **Table 2,** and exhibited the deepest and most robust Fe^{3+}-associated absorption features. All the spectra exhibit H_2O/OH bands near ~ 1400 and ~1900 nm, along with characteristic metal-OH (Fe^{3+}) bands at 2280 and

2400 nm (Bishop et al., 2008b). A slope decrease is present past 2280 nm upon which the Fe-OH absorption band at ~2400 nm is superimposed (**Figure 1**). The center of the NON101-105 absorption band in the 2280 nm region ranges between 2283 nm and 2290 nm (**Figure 1b**); specifically at 2290, 2285, 2286, 2283, and 2288 for NON101-105, respectively (**Table 4**).

In addition to small differences in band positions, the different nontronite samples also exhibit differences in Fe-OH band depths (for an identical grain size), and the presence or absence of a local reflectance maximum in the 780 nm region (**Table 5**). This is likely due to some combination of crystallinity and the presence of additional ferric oxyhydroxides.

4.2 Nontronite versus other phyllosilicates: the 2280-2290 nm band

To determine how spectrally unique nontronite is compared to other minerals, and in particular Fe/Mg phyllosilicates, we conducted an extensive search of the C-TAPE (http://www.uwinnipeg.ca/c-tape) and RELAB (https://sites.brown.edu/relab/relab-spectral-database/) spectral databases. We focused on the presence of a strong 2280 nm absorption feature, a weak or absent 2320 nm absorption feature, and the presence of a distinct 2400 nm absorption feature. We did not find any minerals that exhibit these three properties (**Table 6**). The band centers associated with the metal-OH in other phyllosilicates such as montmorillonite, saponite, and beidellite were present at longer or shorter wavelengths than the 2280-2290 nm nontronite absorption and can be attributed to other cations, such as Al and Mg (Clark et al., 1990). They all displayed a slope drop off longward of their respective absorption band in this wavelength region (**Figures 2a and 2b**).

Hisingerite is of special interest because of its possible confusion with nontronite (Wiens et al., 2022). The hisingerite spectra displayed the closest absorption band center to the 2280 nm nontronite feature, located at 2300, 2290, and 2290 nm for <45 µm sample HIS001, and <75 µm samples c1ph08, and <75 µm c1p09, respectively. The hisingerite spectra display broader and shallower features than nontronite's narrower better-resolved features (Milliken and Bish, 2014), likely attributed to hisingerite's poorly crystalline nature (Eggleton and Tilley, 1998) (**Figures 2b and 3**). Like nontronite, hisingerite displays H_2O/OH features at ~1400 and 1900 nm. The hisingerite spectra exhibit a generally featureless absorption profile in the 1400 nm region, whereas nontronite displays a doublet with centers at ~1415 and ~1430 nm (**Table 4**). The 1900 nm absorption for all nontronite samples was found to be at a shorter wavelength than

hisingerite, from 1903-1910 nm, while hisingerite produced band centers between 1910-1920 nm, demonstrating that hydration-associated absorptions can be used to distinguish these two phyllosilicates. In addition to hydration features, nontronite displays multiple Fe^{3+}-related absorptions in the visible wavelengths of the spectrum, while hisingerite produces a single shallow broad band ~1000 nm (**Figure 3**). Also, unlike nontronite, hisingerite does not exhibit a well-defined 2400 nm absorption band.

The closest mineral we found with the 2280, 2320, and 2400 nm absorption features of nontronite was gibbsite (an aluminum hydroxide: $Al(OH_3)$). It exhibits an absorption band at 2270 nm (~10-15% deep) and a weak or non-existent 2320 nm region band (<2% deep, centered near 2320 nm) (**Figure 4**). This feature is attributable to an Al-OH stretching/bending combination (Cloutis and Bell, 2000).

Nontronite and gibbsite exhibit additional spectral differences, which allow them to be discriminated spectrally. Nontronite will always be accompanied by strong Fe^{3+}-associated absorption features, including the steep reflectance drop-off below ~600 nm, and an absorption band centered near ~900 nm, which are absent in gibbsite spectra. Gibbsite shows a steep reflectance decline longward of ~2100 nm, which is also absent in nontronite. Both minerals exhibit a multi-band absorption feature in the 1400-1500 nm region, but this feature is more complex in gibbsite. The H_2O-related absorption feature near 1900 nm will be a function of H_2O content and hence is not particularly diagnostic, as H_2O is not intrinsic to either mineral. The two minerals could further be discriminated by other means, including composition and structure (e.g., by XRD).

4.3 Nontronite grain size variations – spectral effects

We examined one of our nontronite samples (NON105) as a function of grain size to determine whether grain size-associated spectral changes might mimic spectral differences as a function of composition or heating. The multiple grain size NON105 spectra exhibited an expected decrease in overall reflectance and a more blue-sloped spectrum (i.e., reflectance decreasing toward longer wavelengths) beyond ~1500 nm, as expected. The spectra also show an apparent widening of the ~1400 and 1900 nm H_2O/OH absorption features (**Figure 5**). The Fe^{3+}-associated absorption features below ~1000 nm and the 2280 nm band persist across all grain size spectra (**Figure 5**). The various absorption bands appear to optically saturate (i.e., reach a

maximum band depth) for grain sizes of 106-212 μm (for the 650 1900, 2280, and 2400 nm absorption features), and 212-430 μm for the 900 and 1400 nm absorption features (**Table 5**).

4.4 Heating under Mars-like surface conditions

Some previous experiments (e.g., Che and Glotch, 2010; Morris et al., 2010) showed that nontronite can undergo spectral changes when exposed to temperatures as low as 50°C, while other experiments indicated that major spectral changes can occur above ~400°C (e.g., Che and Glotch, 2012; Gavin and Chevrier, 2010) (summarized in **Table 7**). However, these heating experiments were not conducted under Mars-like surface conditions of pressure and atmospheric composition – a major impetus for this study. Based on the results of these earlier studies, and to better understand the spectrum-altering effects of low-temperature (i.e., ≤300°C) heating on nontronite on Mars, we exposed NON101 (<45 μm grain size) to 110, 180, and 300°C for one week (168 hours) at each temperature in a low-pressure CO_2 environment. Visually, we noticed a shift in visible color from a yellowish-green to a reddish-brown, with increasing temperature, consistent with the formation of hematite or a related Fe-oxyhydroxide.

Additional evidence that both low pressures and heating rates play roles in nontronite alteration comes from previous studies. For example, Ellis and Mortland (1962) found that the decomposition of kaolinite and nontronite, respectively, were affected by the pressure used for thermal decomposition, with lower pressures facilitating dehydration.

The reflectance spectra of the heated nontronite samples are shown in **Figures 7-9**. With increasing temperature, we find progressive spectral changes over the ambient to 180°C range. These include a reduction in the depths of the 650, 900, and 2400 nm Fe^{3+}-OH-associated absorption bands, as well as the 1400 and 1900 nm hydration bands (**Table 5**). The 2280 nm Fe-OH band is quite stable. Upon heating to 300°C, we see more drastic spectral changes: the spectrum is much flatter over the 350-1300 nm interval, the 900 nm Fe-OH band seems to move to shorter wavelengths, and the 1400 and 1900 nm hydration bands are shallower and more featureless. The 2320 and 2400 nm Fe-OH bands are also greatly reduced in intensity.

5. Discussion

The ensuing discussion focuses on how and whether heating to 300°C in a Mars-like surface environment differs from other heating experiments conducted under different

conditions, and how such low-temperature heating can be distinguished from unheated exposure to Mars surface conditions, higher temperature heating, and impact experiments.

5.1 Heating effects on nontronite

Previous studies of nontronite thermal stability have shown that a variety of factors can affect the stability of nontronite. Firstly, robust analysis of nontronite stability is complicated by compositional and structural differences between different samples, the presence of impurities or secondary phases (e.g., Besson et al.., 1983; Bonnin et al., 1985; Che and Glotch, 2012; Ding and Frost, 2002; Gates et al., 2002), and atmospheric pressure (Ellis and Mortland, 1962). The mechanisms associated with the thermal transformation of nontronite and the temperatures at which these occur will be a complex function of factors such as crystallinity, and octahedral site occupancy (e.g., Che and Glotch, 2012; Gavin and Chevrier, 2010; Gavin et al., 2013; Wang et al., 2020 and references therein). The rate of dehydration/dehydroxylation is also time-dependent and controlled by factors such as grain size (e.g., Ding and Frost, 2002) and duration of heating (e.g., Morris et al., 2010).

In general, exposure of nontronite to progressively higher temperatures leads to a number of structural/compositional changes. At the lowest temperatures, nontronite will readily lose adsorbed water as well as interlayer water (largely below ~150° C). Dehydroxylation begins around 350-450°C and extends up to around 700°C. This involves retention of the layered structure of nontronite but also includes loss of hydroxyl, the substitution of hydroxyl by oxygen, and changes in octahedral site configuration (Heller-Kallai and Rozenson, 1980; MacKenzie and Rogers, 1977; Weldon et al., 1982). Between ~700 and 1000°C, previous studies suggest the formation of nanocrystalline and/or poorly crystalline phases. Above ~1000°C, nontronite can recrystallize into cristobalite, sillimanite, and hematite (**Table 7**) (e.g., Che and Glotch, 2012; Ding and Frost, 2002; Gavin and Chevrier, 2010; Gavin et al., 2013). This simple picture of nontronite dehydration and dehydroxylation is complicated by many of the aforementioned factors, so different samples show different temperatures associated with progressive heating (e.g., Ding and Frost, 2002).

The application of multiple analytical techniques enables insights into the structural changes associated with heating. For example, Morris et al., (2010) determined through visible-near infrared spectroscopy, Mössbauer spectroscopy, and X-ray diffractometry the structural

collapse through the complete removal of interlayer H_2O at 210°C. The collapse was determined by the lack of spectral features at 1400 and 1900 nm. However, collapsed nontronite retained the Fe-OH features at 2290 and 2410 nm (Morris et al., 2010).

5.2 The importance of low-temperature heating

As detailed above, exposure of nontronites to low temperatures (<300°C) under Mars-like conditions, leads to a number of spectral changes, which are discussed further below in the context of previous experiments. Low-temperature heating may be an important factor on Mars, and the ability to identify heated nontronites could provide important insights into surface modification processes. There are a number of ways in which nontronites could be heated at low temperatures. These include the burial under ashfall deposits or lava flows (Goudge et al., 2015; Hiesinger and Head, 2004; Mustard et al.,2007, 2009; Tanaka et al., 2014; Kremer et al., 2019), burial under impact ejecta (Barlow, 2005; Michalski and Niles, 2010), or areas away from the immediate point of impact (Abramov and Kring, 2007, 2005, 2004; Osinski et al., 2013; Schwenzer et al., 2012; Schwenzer and Kring 2013).

Heating events on the surface of Mars are widespread with many processes and variables present. The following are several processes but do not limit potential heating determined on the Mars surface: impact heating, impact-generated hydrothermal systems, ejecta, basalt flows, and ashfall deposits are several of the processes seen on Mars that could generate heat and potentially alter minerals. This discussion focuses on the Jezero Crater region's potential heating sources.

Impact-generated hydrothermal systems are proposed for Mars craters (Newsom, 1980; Newsom et al., 1996; Allen et al., 1982) as an environment that may be conducive to life (Schwenzer et al., 2012; Abramov and Kring, 2005). Long-term heating may be an effect of hydrothermal systems generated through impacts as the 4 km diameter Kardla Crater took an estimated 1500-4500 years to cool to temperatures <90 °C (Jõeleht et al., 2005). Daubar and Kring (2001) determined the lifetime of a hydrothermal system in craters from 20-200 km in diameter with exclusively conductive cooling could last up to 103 to 106 years. On planetary bodies whose surfaces are predominantly frozen hydrothermal systems will heat a much larger volume of rock to temperatures above the freezing point of liquid water but <50 °C (Schwenzer et al., 2012).

Mars volcanism is the primary geologic process on the surface throughout the planet's history (Greeley and Spudis, 1981). A large number of basaltic flows are identified on Mars and within the Syrtis Major region. Syrtis Major volcanic complex has associated flows that extend from the central caldera and cover an areal extent of 106 km^2, reaching the western floor of the Isidis basin and covering the Nili Fossae floor (Tornabene et al., 2008). These flows are superposed by ejecta from the Hargraves impact (Mustard et al., 2009).

Impact ejecta can be a source of surface heating outside of the crater rim region. Ejecta blankets typically surround fresh impact craters that extend approximately one to two crater radii beyond the crater rim (Melosh, 1989). Discernable ejecta blankets are attributed to one-third of all martian craters ≥5 km in diameter (Barlow, 2005). Ninety percent of the discernable ejecta blankets possess layered ejecta that have either single or multiple-layer morphologies (Barlow, 2005). Michalski and Niles, (2010) identified a carbonate and phyllosilicate-bearing bedrock exhumed from a depth of 6 km due to a meteorite impact that may have been buried by Syrtis Major volcanic impact ejecta materials.

The pitted capping unit found outside of Jezero Crater is characterized by a relatively thin unit that caps older material with eroded texture and a large number of superposed craters and pits that often contain surficial debris cover (Hiesinger and Head, 2004). It is interpreted as having been formed through volcanic and impact melts from the Isidis basin forming event (Mustard et al., 2007, 2009) that caps the altered basement unit and may be related to older volcanic flows from nearby Syrtis Major (Hiesinger and Head, 2004; Tanaka et al.,2014). The protolith olivine-rich unit has been interpreted as being formed through the exposure of an olivine-rich subsurface layer (Hoefen et al., 2003), olivine-rich basaltic flows (Hamilton and Christensen, 2005), or the emplacement of an olivine-rich impact melt sheet with the formation of the Isidis basin (Mustard et al., 2007, 2009). Jezero Crater exhibits a <10 m thick volcanic floor unit stratigraphically above the period of fluvial activity and the fan deposits (Goudge et al., 2015). The source of this basaltic material is unclear however, is likely attributed to volcanic infill or volcanic resurfaced open basin lakes (Goudge et al., 2012).

The most plausible explanation for the circum–Isidis Planitia olivine-rich unit, one of the most widespread and mineralogically diverse olivine-rich rock units, is that it formed as an

ashfall deposit (Kremer et al., 2019). The ash flow deposit has a probable volcanic origin in the greater Syrtis Major-Isidis Planatia region (Kremer et al., 2019).

Heat tends to decrease at an exponential rate away from the source of the impact (Schwenzer et al., 2012). Large 100-200 km diameter impact events are known to impart kinetic energy from the shock waves that produce and sustain temperatures >90°C in the subsurface for tens of thousands to millions of years (Abramov and Kring, 2007, 2005, 2004). The Sudbury 150 to 250 km diameter or 15,000 km^2 impact structure event produced temperatures up to 1200°C with a large extent of the surrounding rocks only heated to <300°C based on modeling temperatures (Abramov and Kring, 2004, 2005). A 1km thick breccia was deposited over the initial central melt sheet with initial temperatures of 250°C (Abramov and Kring, 2004). Schwenzer et al., (2012) and Abramov and Kring, (2005) used modeling to determine the post-impact temperature distribution of 30 km diameter craters on Mars where the central peak of the crater reaches a temperature of 300-350°C with decreasing temperature over radial and vertical distance. Similar modeling was conducted on 180 km, 100 km, and 14 km diameter craters on Mars (Abramov and Kring, 2005; Schwenzer et al., 2012). The 180 and 100-km diameter craters have modeled temperatures <300°C moving outwards from the central uplift moving from the subsurface and cooling towards the surface (Abramov and Kring, 2005). Small to Medium impact craters up to 20-30 km in diameter both simple and complex will typically range from a maximum of 100-120°C (Osinski et al., 2013). The 14 km diameter crater has a central peak that reaches 50°C (Schwenzer et al., 2012).

Similar heating isotherms may have been produced in the Syrtis Major region on Mars, a heavily cratered terrain. The Isidis basin is a 1900 km diameter impact basin (Schultz and Frey, 1990) from the Late Noachian through age modeling (3.96 Ga) (Werner, 2005). Jezero Crater is a 45 km diameter impact basin (Goudge et al., 2015). Subsequent exhumation of heated nontronites from impact and volcanic processes would then enable their detection on the surface.

Gavin and Chevrier, (2010) found that heating of nontronite, in ambient pressure air or in N_2, suggests that interlayer water is lost at ~400° C; between 400 and 700°C, an intermediate phase, similar to nontronite forms, but with the loss of interlayer water; nanocrystalline and/or poorly crystalline phases formed between 700 and 1000°C; above 1000°C, the sample recrystallized into cristobalite, sillimanite, and hematite (**Table 6**) (Gavin and Chevrier, 2010).

Large changes were seen between ambient conditions and 400°C, with band depths decreasing by factors of 3 to 25 (**Table 5**). All absorption bands essentially disappeared by 725°C. They also noticed a color difference in their nontronite sample heated to 875°C in CO_2 versus air – it was much darker than the other samples, suggesting a possible role of atmospheric composition in the heated alteration of nontronite. However, they also noted no change in reflectance spectra with atmospheric composition (Gavin and Chevrier, 2010).

5.3 Mars surface exposure ± heating

Mars box 1 (MB1), a Mars surface environment exposure experiment of 47 days, was conducted by Cloutis et al. (2007) on several samples, including nontronite (NON101). Exposure to Mars-like surface conditions led to limited spectral variability (**Figure 6**). The Fe-OH-related absorption bands in the <1000 nm region were largely unaffected, while the 1400 and 1900 nm hydration bands showed a measurable reduction in depth but did not completely disappear (**Table 5**). The 2280 and 2400 nm Fe-OH bands were largely unaffected. Exposure to millitorr pressures led to more significant spectral changes: i.e., reduction in the depths of all absorption bands below 2200 nm. However, the 2280 and 2400 nm bands seemed to be largely unaffected by these lower pressures.

The results from this low-pressure exposure have implications for the analysis of Mars meteorites and for Mars sample return. Millitorr pressures from the Mars surface exposure analysis help to constrain the stability of nontronite with relevance to asteroids and delivery of nontronite-bearing samples from Mars to Earth as meteorites. Our results indicate the potential to spectrally identify nontronite in samples exposed to millibar pressure by the persistent 2280-2290 nm absorption band (and with heating no more than 300 °C).

Examination of the "Black Beauty" martian regolith breccia meteorite NWA 7034, shows evidence of impact-induced heating (Goodwin et al., 2022). Goodwin et al. (2022) identified two possible periods of habitability based on the geochronological history of this meteorite, including a pre-Noachian window and an impact-derived hydrothermal system allowing for habitable crater environments in the Amazonian (Goodwin et al., 2022). The meteorite experienced a lithifying disturbance event ~ ca. 1500 Ma with a bulk temperature excursion below 900°C, along with exposure to 700°C for weeks to years post-impact, while buried >5m deep in an impact blanket (Goodwin et al., 2022). NWA 7034 showed additional evidence of hydrothermal

alteration - from feldspar veins cross-cutting previously oxidized clasts indicating hot fluids in contact with breccia to temperatures >500°C (MacArthur et al., 2019). Our study demonstrates that the potential to identify nontronite in any meteorite at temperatures lower than or equal to 300°C is likely using the characteristic Fe-OH 2280-2290 nm features. However, based on previous heating results past 300°C, the extensive heating and alteration undergone by NWA 7034 would likely dehydrate and alter any nontronite beyond the point where its diagnostic spectral features would persist. Any nontronite detected in such a sample would more plausibly be attributable to terrestrial alteration, post-impact hydrothermal systems (Schwenzer and Kring, 2009), or have been excavated from deeper layers by the impact (Mangold et al., 2007; Gavin et al., 2013). To determine these possible modification processes, wet heating experiments are planned that may constrain hydrothermal alteration.

5.4 Atmospheric pressure and compositional effects on heating

Heating nontronite at low pressure is expected to promote dehydration (Ellis and Mortland, 1962). Comparison of our results to some previous studies allows us to partially disentangle the effects of heating in different conditions. However, only a limited number of studies included heating below ~300°C (Morris et al., 2010; Che and Glotch, 2012) (**Table 5**).

Ding and Frost (2002) have suggested that the type of atmosphere in which nontronite is heated could lead to the formation of ferric phases and/or other phases whose abundances would be too low to detect by many analytical techniques but which could lead to spectroscopic changes (e.g., maghemite) (MacKenzie and Rogers, 1977; Moskowitz and Hargraves, 1984; Hviid et al., 1994).

Morris et al. (2010) investigated nontronite heated in N_2 at ambient pressures at 50, 105, and 210°C, and found that interlayer water was lost above ~210°C; spectrally this was seen as a loss of 1400 and 1900 nm region OH/H_2O bands. The Fe^{3+}-associated bands below ~1000 nm were lost upon heating to between 105° and 210°C. Even upon heating to 50°C, they found a reddening of the red slope below ~1200 nm (**Table 6**). As with our results, the most persistent spectral features were the Fe-OH absorption bands in the 2280 and 2400 nm regions. At 105°C (heating for 1004 hours) all the nontronite-associated absorption bands disappeared.

Che and Glotch (2012) heated pressed pellets of nontronite in H_2O- and CO_2-purged ambient terrestrial atmosphere to temperatures of between 100 and 900°C in 100°C increments. They measured reflectance spectra above 1200 nm, and found no systematic spectral changes below 300°C; the 1400 nm OH band disappeared by 400°C, while the 1900 nm H_2O band changed shape at 400°C and disappeared by 700°C; the 2280 and 2400 Fe-OH bands were largely unchanged to 300°C, and then weakened and disappeared by 700°C. DSC curves showed minima at either 109 or 138° C and a maximum of around 850°C.

The Morris et al. (2010) and Che and Glotch (2012) studies are closest in conditions to our study, at least in terms of the temperature range. A comparison of their results to ours suggests that heating in a low-pressure CO_2 environment promotes dehydration and loss of OH and H_2O, as both bands weaken at 110°C. While these study results are not directly comparable, it appears that dehydration and loss of water occur around 130-210°C, loss of the Fe-OH bands in the 2280 and 2400 nm region occur above 300°C, and some change in OH-bonded Fe^{3+} can occur as low as 50-100°C as evidenced by changes in spectral slope and the position, width, and depth of Fe^{3+}-associated absorption bands below 1000 nm of the Morris et al. (2010) spectra.

5.5 Duration of heating effects

We exposed our nontronite sample to heating for 1 week (168 hours) at each temperature increment (110, 180, 300°C). This was done to try and ensure that any compositional-structural-spectral changes would be complete by this time. This time interval was informed by our previous low-pressure exposure experiments (Cloutis et al., 2007).

Morris et al. (2010) found spectral changes occurring over periods of days to weeks for their nontronite samples held at a constant temperature, with increasing time leading to loss of the Fe^{3+}-associated absorption features and hydration bands near 1400 and 1900 nm, as well as the Fe-OH bands below 1000 nm. As found by Morris et al. (2010), we found similar significant spectral changes at the lowest temperature (110°C) investigated. This is in contrast to shorter-term heating experiments (one day per temperature increment - Che and Glotch, 2012; **Table 7**) where spectral changes are largely confined to temperatures >400°C. Their results for their two nontronite samples show disparate results (**Table 5**). One sample showed an initial increase in all band depths, followed by a decrease, while the other showed little change to 200°C and then

modest decreases to 300°C (from ambient temperature to 300°C). None of the absorption bands disappeared by 300°C (**Table 5**).

It is difficult to disentangle the effects of atmospheric pressure, atmospheric composition, and duration of heating, but it would appear that all three play a role in nontronite decomposition, with the duration of heating being the most important factor (for a constant temperature). This has implications for the spectrum-altering effects of transient versus long-duration heating.

5.6 Heating versus shock heating

There are multiple shock experiments involving nontronite. These experiments allow the combined effects of pressure plus temperature to be investigated and are directly relevant to how impacts can affect the structural, compositional, and spectroscopic properties of nontronites.

Boslough et al. (1980) conducted shock experiments (18-30 GPa) in air on pressed powders of <63 µm nontronite. They found that the major effects of shock were the collapse of the nontronite along the c-axis, associated with loss of interlayer water. They also noticed a substantial decrease in OH content. Boslough et al. (1986) compared thermally annealed to shocked nontronites. They found that for samples heated above 600°C, there was very little structural similarity to the shocked samples. They attributed this to the formation of new and different phases between them.

Weldon et al. (1982) found that nontronite samples heated in a reducing environment had a visual appearance and Mössbauer spectra that were unlike impacted samples subjected to similar temperatures (~350 and ~550°C); however, these differences were not investigated in detail. In their shock experiments, they determined that partial dehydroxylation occurred, and the post-impact octahedral site was a mixture of 4-, 5-, and 6-fold coordination, due to a loss of OH. This caused the Fe-O absorption edge to shift further into the visible spectral region, manifested as a darker and redder sample. It was also concluded that the bulk of the sample did not experience temperatures high enough (i.e., ~300°C) to promote thermal dehydroxylation.

Gavin et al. (2013) conducted laboratory shock experiments on <63 µm nontronite powders in ambient air (**Table 5**). The temperatures that the samples experienced ranged from 80-137°C (average) and 220-524°C (peak); pressures were 0.9-1.6 GPa (average) and 5.4-17.5

GPa (peak). They found that with increasing shock pressures and temperatures, the 1400 and 1900 nm hydration bands increased slightly in strength, the color of the samples was unaffected, the 2280 and 2400 nm Fe-OH bands were unaffected, and a new band appeared at 2100 nm (**Table 7**). Their spectra do show a shallower spectral slope in the 1100-1300 nm region for the most shocked sample. Spectral changes were more noticeable in the mid-infrared than in the 1000-2500 nm region.

Friedlander et al. (2015) conducted laboratory impact shock experiments on <2 µm nontronite as pressed powders (**Table 7**). They were subjected to peak pressures of 10.2-39.1 GPa. As with Gavin et al. (2013), they found that the 1400 and 1900 nm hydration bands persisted to the highest pressures, but were weakened (**Table 5**). The spectra became gradually redder and the 2280 nm band shifted to slightly shorter wavelengths, while the 2400 nm band shifted to slightly longer wavelengths; both bands gradually broadened and disappeared at pressures of 34.6 GPA, likely due to distortion of crystallographic sites and partial loss of hydroxyl. Of the <1000 nm bands, the 650 nm Fe-OH band was the first to disappear (at somewhere above 10.2 GPa), while the 950 nm Fe-OH band persisted to the highest pressures, albeit weaker and broader. Friedlander et al. (2016) found that dioctahedral smectites were more susceptible to structural deformation than trioctahedral smectites, likely due to the site vacancies in the former.

Michalski et al. (2017) also conducted shock experiments on fine-grained (<2 nm) nontronite powders pressed into pellets. The shock experiments were conducted in air, with pressures between 10 and 40 GPa (**Table 5**). They found a decrease in the depth of the 2280 nm Fe-OH absorption band with increasing pressure, with the band disappearing at ~35 GPa (**Table 5**). The 2400 nm Fe-OH band blended into the overall decrease in reflectance towards longer wavelengths by ~10 GPa. The 1400 and 1900 nm hydration bands were present in all the samples, but with generally lower intensities. They concluded that while the spectra do change, overall, the ability to detect nontronite was not unduly affected.

Kraus et al. (2013) found that it is difficult to interpret the results of laboratory shock experiments and to extrapolate them to impact shocks on planetary surfaces.

5.7 Heating versus shock (heating) on nontronite reflectance spectra

Differences between heated versus shocked nontronites were noted by Boslough et al. (1986). Obvious differences exist between long-term (hours to weeks) laboratory heating of nontronites versus shock-associated heating (less than a few minutes). Also, shock experiments involve changes in pressure that can affect the structure of nontronites (e.g., Gavin et al., 2013; Friedlander et al., 2015). These differences are manifested as differences in some spectral properties. Heated nontronite can begin to show spectral differences at 50°C, such as reddening (Morris et al., 2010), followed by changes in the Fe^{3+}-associated absorption bands, located below 1000 nm, between 50 and 105°C, and loss of these bands and hydration bands between 105 and 210°C.

For the shock experiments, hydration bands in the 1400 and 1900 nm persist in almost all the shock sample spectra whereas they are largely lost by 200-300°C in the heating experiments. This may be attributable to the short duration of heating associated with the shock experiments, whereby any liberated water cannot escape from the samples prior to cooling. Also, the 950 nm Fe-OH band persists to pressures of at least 39.1 GPa (Friedlander et al., 2015), while the 650 nm Fe-OH band is lost at low pressures. The 2,280 nm Fe-OH band also persists to somewhere around 30 GPa (**Table 5**).

It is difficult to directly compare the results of the impact experiments to the heating experiments, as the shock experiments result in a range of temperatures (e.g., Gavin et al., 2013), and temperature estimates are not provided in the other cited studies (Friedlander et al., 2015; Michalski et al., 2017). Nevertheless, the major spectral differences relate to the preservation of 1400 and 1900 nm bands in the shock experiments over a wide range of shock pressures. It is worth noting that impact experiments will disrupt the crystalline structure of nontronite due largely to pressure-associated effects (Friedlander et al., 2015), whereas heating will disrupt the structure due to the loss of hydroxyl and H_2O. This, in turn, will manifest itself as a reduction in 1400 and 1900 nm OH/H_2O absorption bands, as well as for the various absorption bands associated with hydroxide-bridged Fe. As noted by Gavin et al. (2013), it is difficult to disentangle the sample alteration effects associated with shock pressures versus temperature. They also noted that in laboratory shock experiments, shock affects essentially the entire sample, while elevated temperatures are much more localized.

5.8 The "disappearance" of absorption bands

The term disappearance, when referring to the absence of an absorption band in a spectrum can be a misnomer. In the case of nontronite spectra, the "disappearance" of an absorption band can be due to a number of causes (e.g., Morris et al., 2010). As an example, the various Fe^{3+}-OH bands could "disappear" when bridging OH is lost from the structure (dehydroxylation), the structure changes to the point that there is a wider range of Fe-OH bond length so that the band becomes broader and shallower to the point of not being detectable. This could happen via dehydroxylation or dehydroxylation accompanying shock alteration of nontronite's crystal lattice. An absorption band could also become indistinguishable as a result of the formation of opaque phases that lower reflectance sufficiently to "hide" an absorption band. In a similar vein, an absorption band could become "masked" by an adjacent feature, such as the strong Fe-O charge transfer band that can become increasingly intense and wide from impact shock (e.g., Weldon et al., 1982).

5.9 Other wavelength regions

In addition to spectral differences between shocked and heated nontronites, additional insights into the nature of nontronites on Mars could be learned from the comparison of results from different wavelength regions. As noted by Che and Glotch (2012), Gavin et al. (2013), Friedlander et al. (2015), Michalski et al. (2017), and others, different wavelength regions are sensitive to different properties of nontronite. For example, the visible-near infrared region is sensitive to properties such as OH/H_2O content and Fe hydration state and bonding, while the mid-infrared region is more sensitive to the silicate lattice.

6. Implications for nontronite on Mars

Many of the experiments described in this paper were designed to enable the detection of nontronites on Mars and to better understand the conditions to which they had been exposed. A review of these studies is outside the scope of this paper. We note here that our study is complementary to them, and heating was conducted under more Mars-like conditions.

For visible-near infrared spectra, nontronite detection has been largely based on the presence of an absorption feature in the 2300 nm region. Our results and analysis suggest that the narrow 2280 nm Fe-OH absorption band is the most persistent and diagnostic absorption feature associated with nontronite. We also note that little to no Mg can be incorporated into nontronite's

dioctahedral structure (e.g., Petit et al., 2017). Mg-bearing phyllosilicates have a narrow absorption feature near 2320 nm (**Table 6**; Clark et al., 1990). This suggests that nontronites are spectrally distinct from other Fe/Mg phyllosilicates.

Fairen et al. (2010) determined areas associated with different-sized craters where temperatures would not exceed those associated with visible-near infrared spectral detectability. As we have demonstrated, spectral detectability is a function of temperature even at temperatures below that associated with nontronite dehydroxylation, so that detectability is a wavelength-specific term, and spectral differences associated with temperature could be used to constrain temperatures.

Pelkey et al. (2007) developed a number of spectral parameters to enable the detection and characterization of absorption bands associated with various minerals of interest on Mars. Of most relevance is "BD2290", which measures the depth of any absorption feature in the 2300 nm region. It uses a continuum from 2250 to 2350 to detect an absorption band in this region and is intended for Mg, and Fe-OH minerals. As noted in this study, this wavelength region covers both the 2280 nm Fe-OH band as well as the 2320 nm Mg-OH band, so it is not able to discriminate nontronite from Mg-bearing phyllosilicates.

A number of previous studies have identified what are termed Fe/Mg smectites on Mars, on the basis of an absorption band in the 2300 nm region. Poulet et al. (2005) identified the presence of Fe/Mg smectites on the basis of an absorption band in the 2300 nm region. They attributed variations in band shape to varying Fe/Mg abundances.

Bibring et al. (2005) used OMEGA data to identify the presence of nontronite on the basis of its characteristics 2280 nm Fe-OH band across Mars. Additional bands were also seen at 2400 nm, as well as in the 1400 and 1900 nm regions. They noted that nontronite was the most abundant phyllosilicate detected by OMEGA.

Loizeau et al. (2007) used OMEGA spectra to characterize phyllosilicates in the Mawrth Vallis region of Mars. They identified outcrops with a 2300 nm region absorption feature that they attributed to nontronite. However, its band is shifted to longer wavelengths than nontronite, and the position of the 1900 nm absorption band and doublet of the 1400 nm band are not aligned with the OMEGA spectra.

Bishop et al. (2008a) and Wray et al. (2008) examined CRISM spectra to better constrain the nature of phyllosilicates in the Mawrth Vallis region. They both detected a number of occurrences of a 2300 nm absorption feature that they attributed to Fe/Mg-smectites. As we have concluded, these probably represent a mixture of nontronite and Mg-phyllosilicates.

Le Deit et al. (2012) conducted a similar spectroscopic survey around Valles Marineris and noted 4 different formation types associated with clays. They compared CRISM spectra to laboratory spectra of nontronite, saponite, and vermiculite to try and constrain specific clay types. They concluded that the detected clays on the basis of a 2300 nm region absorption feature are of mixed types.

McKeown et al. (2009) applied the parameters of Pelkey et al. (2007) – i.e., BD2300 – to characterize phyllosilicates in the central Mawrth Vallis region. They mentioned the detection of a more Mg-rich nontronite, which we suggest, is more likely a mixture of nontronite and Mg-OH phyllosilicates, as nontronite is not able to incorporate Mg into its dioctahedral structure (e.g., Petit et al., 2017). They also identified nontronite on the basis of a 2280 nm absorption band in some of their CRISM spectra; the spectra also included 1400 and 1900 nm hydration bands, but not the shorter wavelength nontronite bands. As we have noted, the shorter wavelength bands are the first to disappear upon heating. They also mentioned that nontronite is the most common phyllosilicate identified in the Mawrth Vallis region.

As demonstrated by a number of these studies, the inclusion of geomorphological and stratigraphic information, as well as multiple wavelength regions, can provide clearer insights into the origin, evolution, emplacement, and thermal and shock history of nontronite-bearing deposits.

For current instruments on Mars, nontronite detection is possible using multiple techniques. Spectral resolutions between orbital and lab-based detections of nontronites on Mars are different. The lab-based ASD at C-TAPE has a 7 nm spectral resolution compared to CRISM which has a 10 nm spectral resolution with a larger sampling interval making detections between nontronite and hisingerite far more ambiguous through orbital detections. The Mars Bidziil target indicates a similar spectrum to our nontronite samples with the 2280 nm band with a slope decrease towards the 2240 nm in both Fe-OH absorption bands (Wiens et al., 2022). Additionally, the target exhibits well-defined hydration bands at 1420 and 1920 (Wiens et al.,

2022). Beyond reflectance and XRD, discussed above, Laser-Induced Breakdown Spectroscopy (LIBS) analysis would be able to determine the aluminum content (lower in hisingerite) which would provide adequate information to determine mineralogy.

Any plausible detections based on orbital data would likely need to be accompanied by additional in situ analysis and sample return missions to confirm the presence of nontronite in locations such as Jezero Crater. The CRISM and OMEGA detections of nontronite are based on the absorption bands at ~1900 and 2300 nm (Ehlmann et al., 2008; Mustard et al., 2008; Poulet et al., 2005). Issues with these identifications lie in the spatial resolution which is less problematic for landed instruments (Milliken and Bish, 2014). From our results, the position of the 2300 nm band could potentially be attributed to nontronite due to its characteristic absorption band at 2280-2290 nm, though a mixture or the presence of another phyllosilicate such as saponite or hisingerite may not be ruled out. Hisingerite and nontronite detection could be interpreted similarly (even at scales smaller than CRISM and OMEGA resolution) because the olivine/pyroxene vs. plagioclase abundance can vary over these scales – this seems apparent from observations at Jezero (Wiens et al. 2022). Several minerals also exhibit absorption bands in the 2300 nm region (e.g., Clark et al., 1990), which would further complicate the identification of nontronite. Nontronite may be detected using several of the mentioned techniques, therefore the results of this study can be used to further constrain the alteration history of processes such as impact heating, formation of hydrothermal systems, and volcanism of samples and/or targets on Mars.

7. Summary

Because dehydroxylation proceeds at generally higher temperatures than dehydration, OH-associated absorption bands will persist to higher temperatures (and higher shock pressures) than H_2O-associated absorption bands. In addition, Fe-OH bonds that involve a single Fe atom and a single OH molecule should be more resistant to degradation than those involving two Fe atoms and a bridging OH. In the case of nontronite, the single Fe atom-associated absorption band is the 2280 nm feature, while the absorption features below 1000 nm involve two Fe atoms bridged by OH (e.g., Sherman and Vergo, 1988). This likely accounts for the fact that the 2280 nm absorption feature becomes shallower at a slower rate with increasing temperature than the features below 1000 nm. This indicates that the 2280 nm band is the best feature for identifying

the presence of nontronite. In addition, we have shown that this absorption feature is unique to nontronites.

Some of the major findings from our study, and comparison to previous research suggest that the 2280 nm Fe-OH band is the most persistent absorption band in 350-2500 nm nontronite spectra, being most resistant to heating and shock. However, its depth does decrease with increasing temperatures (even below the generally accepted dehydroxylation temperature of ~400°C). This suggests that partial dehydroxylation occurs at these "lower" temperatures. Because this band is associated with a single Fe atom and single OH molecule, it is less likely to be altered as compared to other Fe-associated molecules that involve two Fe atoms and a bridging OH molecule. This accounts for the fact that lower wavelength absorption bands (<1000 nm) that involve such double bonds are less likely to persist at higher temperatures. Some change in the structure of nontronite with increasing temperature is also implied by the gradual loss of detail in the 1400 nm region.

Our results suggest that nontronite is relatively stable under Mars surface conditions, and to heating to at least 300°C in terms of the persistence of a 2280 nm Fe-OH band, while Fe^{3+}-associated absorption bands below ~1000 nm are strongly altered as low as 110°C. Similarly, the 1400 and 1900 nm H_2O/OH-related absorption bands are present, albeit weakly in the 300°C spectra, suggesting that some hydrated interlayers of nontronite would persist on the martian surface in both heated and unheated nontronites (Cloutis et al., 2007). Therefore, the scenario of organics being sheltered and protected in the extreme environments on Mars within the phyllosilicate layers is plausible. Due to the spectral stability of nontronite up to 300°C under Mars-like pressures under purged CO_2, exposure to Mars-like surface and millibar pressure conditions determined in this study, identifying nontronite on Mars can aid in determining locations of possible concentrations of organic molecules due to nontronite's water and organic molecule retention properties and its ability to protect organics from thermal and UV destruction (Poch et al., 2015; dos Santos et al., 2016), oxidation, or metabolization (Kennedy et al., 2002; Williams et al., 2005).

Nontronite is also an important mineral to identify on Mars due to its implications for environmental conditions present during formation, and subsequent stability (Grotzinger, et al., 2012; Tu, et al., 2021). Dissolution rates are determined for long-term nontronite stability and

secondary precipitates forming sediments on the martian surface. The Gainey et al., (2014) experiment indicates that nontronite is likely to persist under aqueous conditions on Mars and once formed would persist for prolonged periods relative to the surrounding basalt. The dissolution rates from laboratory experiments follow the same order in the field, therefore are comparative (Hausrath et al., 2008a, 2008b). The paleoclimate of Mars is still debated, with anoxic surface conditions likely being present on early Mars (Chetomb et al., 2017). The timing of the evolution to current oxidizing conditions is unresolved (Chevrier et al., 2007; Carr and Head, 2010; Catling and Moore, 2003; Ramirez et al., 2014; Sholes et al., 2017). The current formation of nontronite on Mars may result in unfavorable conditions for organic matter as a result of the current oxidizing environment (Gainey et al., 2017). However, anoxic conditions may have persisted beyond the Noachian due to the presence of ferric smectites in late Noachian sedimentary units detected in situ at Gale crater by the Curiosity rover and from orbit (Milliken et al., 2010; Murchie et al., 2009; Mustard et al., 2008; Poulet et al., 2008, 2014). This also indicates the potential for organics to be hosted within the smectite layers during past habitable periods on Mars.

Studies indicate that the formation of nontronites can occur over a wide range of temperatures and time. However, nontronites can exhibit structural differences as the time and temperature of synthesis vary: Baker and Strawn (2014) found that nontronites synthesized over 28 days up to temperatures of 150°C are less crystalline when compared to natural nontronite samples collected from the Columbia River, which were likely formed under lower temperatures and over longer periods (Baker and Strawn, 2014).

The RELAB Beaver Bay analog site samples c1ph08 and c1p09 <75 µm grain size spectra were collected from an iron-rich gabbroic bedrock with fayalitic olivine and iron-rich pyroxene producing poorly crystalline hydrous silicate hisingerite by deuteric and late-stage hydrothermal alteration (Burns, 1986; Whelan and Goldich, 1961). Hisingerite and nontronite formation conditions are similar with both being able to form under low temperatures due to weathering of basaltic bedrock and as hydrothermal alteration minerals. Both could be identified in the region of Fe-rich basalts with weathering products such as serpentine and talc that have formed within the same process.

Nontronite detection is best accomplished using the presence of a sharp ~2280-2290 nm band and a weak or absent 2320 nm band. As mentioned, nontronites are the only phyllosilicates we examined with these spectral characteristics (**Table 6**), which usually provides a diagnostic determination for Mars surface detections. Relatively pure hisingerite can be spectrally identified based on the presence of its broader band centered at a longer wavelength (2290-2300 nm), however, if present in a mixture or as assemblages, identification may be more problematic (Milliken and Bish, 2014). The CheMin instrument on the Curiosity Rover has the ability to differentiate these minerals based on the peaks present in the XRD patterns (Milliken and Bish, 2014). Milliken and Bish, (2014) highlighted the difficulties of determining hisingerite from nontronite spectra using only VIS-NIR spectra as the band centers are relatively close, with a small spectral difference due to the amorphous nature of hisingerite producing a broader Fe-OH absorption. However, our study has demonstrated that nontronite versus hisingerite discrimination is possible. The discrimination is based on the characteristic 2280-2290 nm feature along with the H_2O/OH hydration centers and the likely additional Fe-OH absorption near 2400 nm. Other minerals lack a strong 2280-2290 nm absorption band, with the closest match being gibbsite. However, as discussed above, there are multiple other spectral differences

Heating to between 180 and 300°C, which may be due to impact-induced heating, did not affect most of the nontronite's characteristic absorption features. Our results indicate the stability and robustness of the characteristic spectral features of nontronite present at ~1900 nm and 2280-2290 nm after exposure to Mars surface-like conditions and after heating to >180°C. Our results indicate that the current surficial occurrences of nontronite, and possibly other Fe-smectites, on Mars have not undergone impact-induced heating past the point of nontronite spectral decomposition (>180°C).

Our heating experiments were conducted in an enclosed vacuum oven under 20-100 millibar purged with CO_2 to simulate early Mars surface conditions. Our experiments are consistent with comparable previous thermal studies of nontronite. Our results also fill a gap of temperatures below ~350 °C and the threshold of nontronite spectral dehydroxylation

8. Conclusion

The results from this study can be used to interpret the presence of nontronite using spectroscopic orbital observational data from OMEGA and CRISM, in addition to in-situ rover

detections on the martian surface. Observations of nontronite have implications for past environmental conditions due to their restricted formation conditions and their ability to trap and synthesize organics. The effects of grain size variations, heating up to 300°C (which may be caused by impact heating events) and exposure to Mars simulated environment demonstrated the spectral robustness and uniqueness of the ~2280-2290 nm absorption feature. Our results both demonstrate and confirm that the Fe-OH feature associated with nontronite is unique and spectrally stable under Mars-like surface conditions, moderate heating, and millibar pressures.

Acknowledgments

This study was supported with funding from the Canadian Space Agency, the Natural Sciences and Engineering Research Council of Canada, the Canada Foundation for Innovation, the Manitoba Research Innovation Fund, and the University of Winnipeg. S. Mertzman thanks the NSF-MRI Program for XRF Instrumentation support (NSF- EAR 1872311) and Karen R. Mertzman for her ongoing meticulous work in the lab. T. Fornaro would like to acknowledge the Italian Space Agency (ASI) grant agreement ASI/INAF n. 2017-48-H-0. We wish to thank Dr. Benjamin Tutolo and an anonymous reviewer for their comments that greatly improved the manuscript.

References

Abramov, O. and Kring, D.A., 2004. Numerical modeling of an impact-induced hydrothermal system at the Sudbury crater. *Journal of Geophysical Research: Planets*, *109*(E10).

Abramov, O. and Kring, D.A., 2005. Impact-induced hydrothermal activity on early Mars. *Journal of Geophysical Research: Planets*, *110*(E12).

Abramov, O. and Kring, D.A., 2007. Numerical modeling of impact-induced hydrothermal activity at the Chicxulub crater. *Meteoritics & Planetary Science*, *42*(1), pp.93-112.

Adams, J. M. 1983., Reactions of alcohols with alkenes over an aluminum-exchanged montmorillonite. *Clays and Clay Minerals*, *31*(2), pp.129–136. https://doi.org/10.1346/CCMN.1983.0310207

Allen, C.C., Gooding, J.L. and Keil, K., 1982. Hydrothermally altered impact melt rock and breccia: Contributions to the soil of Mars. *Journal of Geophysical Research: Solid Earth*, *87*(B12), pp.10083-10101.

Baker, L. L., and Strawn, D. G. 2014., Temperature effects on the crystallinity of synthetic nontronite and implications for nontronite formation in Columbia River basalts. *Clays and Clay Minerals*, *62*(2), pp.89–101. https://doi.org/10.1346/CCMN.2014.0620202

Barlow, N.G., 2005. A review of Martian impact crater ejecta structures and their implications for target properties. *Large meteorite impacts III*, *384*, pp.433-442.

Besson, G., Bookin, A.S., Dainyak, L.G., Rautureau, M.T.S.L., Tsipursky, S.I., Tchoubar, C.T. and Drits, V.A., 1983. Use of diffraction and Mössbauer methods for the structural and crystallochemical characterization of nontronites. *Journal of Applied Crystallography*, *16*(4), pp.374-383.

Bibring, J.P., Langevin, Y., Gendrin, A., Gondet, B., Poulet, F., Berthé, M., Soufflot, A., Arvidson, R., Mangold, N., Mustard, J. and Drossart, P., 2005. Mars surface diversity as revealed by the OMEGA/Mars Express observations. *Science*, *307*(5715), pp.1576-1581.

Bibring, J.P., Langevin, Y., Mustard, J.F., Poulet, F., Arvidson, R., Gendrin, A., Gondet, B., Mangold, N., Pinet, P., Forget, F. and Berthé, M., 2006. Global mineralogical and aqueous Mars history derived from OMEGA/Mars Express data. S*cience*, *312*(5772), pp.400-404.

Bishop, J.L., Pieters, C.M. and Edwards, J.O., 1994. Infrared spectroscopic analyses on the nature of water in montmorillonite. *Clays and clay minerals*, *42*(6), pp.702-716.

Bishop, J., Murad, E. and Dyar, M.D., 2002a. The influence of octahedral and tetrahedral cation substitution on the structure of smectites and serpentines as observed through infrared spectroscopy. *Clay Minerals*, *37*(4), pp.617-628.

Bishop, J., Madejová, J., Komadel, P. and Fröschl, H., 2002b. The influence of structural Fe, Al and Mg on the infrared OH bands in spectra of dioctahedral smectites. *Clay minerals*, *37*(4), pp.607-616.

Bishop, J.L., Dobrea, E.Z.N., McKeown, N.K., Parente, M., Ehlmann, B.L., Michalski, J.R., Milliken, R.E., Poulet, F., Swayze, G.A., Mustard, J.F. and Murchie, S.L., 2008a. Phyllosilicate diversity and past aqueous activity revealed at Mawrth Vallis, Mars. *Science*, *321*(5890), pp.830-833.

Bishop, J.L., Lane, M.D., Dyar, M.D. and Brown, A.J., 2008b. Reflectance and emission spectroscopy study of four groups of phyllosilicates: Smectites, kaolinite-serpentines, chlorites and micas. *Clay Minerals, 43*(1), pp.35-54.

Bishop, J.L., Gates, W.P., Makarewicz, H.D., McKeown, N.K. and Hiroi, T., 2011. Reflectance spectroscopy of beidellites and their importance for Mars. *Clays and Clay Minerals, 59*(4), pp.378-399.

Bishop, J.L., Tirsch, D., Tornabene, L.L., Jaumann, R., McEwen, A.S., McGuire, P.C., Ody, A., Poulet, F., Clark, R.N., Parente, M. and McKeown, N.K., 2013. Mineralogy and morphology of geologic units at Libya Montes, Mars: Ancient aqueously derived outcrops, mafic flows, fluvial features, and impacts. *Journal of Geophysical Research: Planets, 118*(3), pp.487-513.

Bonnin, D., Calas, G., Suquet, H. and Pezerat, H., 1985. Sites occupancy of Fe3+ in Garfield nontronite: a spectroscopic study. *Physics and Chemistry of Minerals, 12*(1), pp.55-64.

Boslough, M.B., Weldon, R.J. and Ahrens, T.J., 1980. Impact-induced water loss from serpentine, nontronite and kernite. *In Lunar and Planetary Science Conference Proceedings* (Vol. 11).

Boslough, M.B., Venturini, E.L., Morosin, B., Graham, R.A. and Williamson, D.L., 1986. Physical properties of shocked and thermally altered nontronite: Implications for the Martian surface. *Journal of Geophysical Research: Solid Earth, 91*(B13), pp.E207-E214.

Brossier, J., Altieri, F., De Sanctis, M.C., Frigeri, A., Ferrari, M., De Angelis, S., Apuzzo, A. and Costa, N., 2022. Constraining the spectral behavior of the clay-bearing outcrops in Oxia Planum, the landing site for ExoMars "Rosalind Franklin" rover. Icarus, 386, p.115114.

Brown, A.J., Hook, S.J., Baldridge, A.M., Crowley, J.K., Bridges, N.T., Thomson, B.J., Marion, G.M., de Souza Filho, C.R. and Bishop, J.L., 2010. Hydrothermal formation of clay-carbonate alteration assemblages in the Nili Fossae region of Mars. *Earth and Planetary Science Letters, 297*(1-2), pp.174-182.

Brown, A. J., Viviano, C. E. and Goudge, T. A. 2020, Ancient Australian Rocks and the Search for Life on Mars. https://doi.org/10.48550/arXiv.2007.06656

Burns, R.G., 1986, March. Hisingerite and iddingsite: Deuteric alteration products of basalts on Mars. In *Lunar and Planetary Science Conference* (Vol. 17, pp. 93-94).

Clark, R. N., & Roush, T. L., 1984. Reflectance spectroscopy: Quantitative analysis techniques for remote sensing applications. *Journal of Geophysical Research: Solid Earth, 89*(B7), pp.6329–6340. https://doi.org/10.1029/JB089iB07p06329

Clark, R.N., King, T.V., Klejwa, M., Swayze, G.A. and Vergo, N., 1990. High spectral resolution reflectance spectroscopy of minerals. *Journal of Geophysical Research: Solid Earth, 95*(B8), pp.12653-12680.

Clark, R.N., Swayze, G.A., Wise, R.A., Livo, K.E., Hoefen, T.M., Kokaly, R.F. and Sutley, S.J., 2007. *USGS digital spectral library splib06a* (No. 231). US Geological Survey.

Carr, M. H., & Head, J. W. III., 2010. Geologic history of Mars. *Earth and Planetary Science Letters, 294*, pp.185–203. https://doi.org/10.1016/j.epsl.2009.06.042

Carter, J., Poulet, F., Bibring, J. P., Mangold, N., Murchie, S, 2013. Hydrous minerals on Mars as seen by the CRISM and OMEGA imaging spectrometers: Updated global view. *Journal of Geophysical Research: Planets*, *118*, pp. 831-858.

Catling, D. C., & Moore, J. A., 2003. The nature of coarse-grained crystalline hematite and its implications for the early environment of Mars. *Icarus*, *165*(2), pp.277–300. https://doi.org/10.1016/S0019-1035(03)00173-8

Chemtob, S.M., Nickerson, R.D., Morris, R.V., Agresti, D.G. and Catalano, J.G., 2017. Oxidative alteration of ferrous smectites and implications for the redox evolution of early Mars. *Journal of Geophysical Research: Planets*, *122*(12), pp.2469-2488.

Chevrier, V., Poulet, F., & Bibring, J.-P., 2007. Early geochemical environment of Mars as determined from thermodynamics of phyllosilicates. *Nature*, 448, pp.60–63. https://doi.org/10.1038/nature05961

Che, C. and Glotch, T., 2010, March. The effect of high temperatures on the emission and VNIR reflectance spectra of phyllosilicates and zeolites. In *41st Annual Lunar and Planetary Science Conference* (No. 1533, p. 1513).

Che, C. and Glotch, T.D., 2012. The effect of high temperatures on the mid-to-far-infrared emission and near-infrared reflectance spectra of phyllosilicates and natural zeolites: Implications for Martian exploration. *Icarus*, *218*(1), pp.585-601.

Clark, R.N., King, T.V., Klejwa, M., Swayze, G.A. and Vergo, N., 1990. High spectral resolution reflectance spectroscopy of minerals. *Journal of Geophysical Research: Solid Earth*, *95*(B8), pp.12653-12680.

Clark III, B.C., Arvidson, R.E., Gellert, R., Morris, R.V., Ming, D.W., Richter, L., Ruff, S.W., Michalski, J.R., Farrand, W.H., Yen, A. and Herkenhoff, K.E., 2007. Evidence for montmorillonite or its compositional equivalent in Columbia Hills, Mars. *Journal of Geophysical Research: Planets*, *112*(E6). https://doi.org/10.1029/2006JE002756

Cloutis, E.A., and J.F. Bell III., 2000. Diaspores and related hydroxides: Spectral-compositional properties and implications for Mars. *Journal of Geophysical Research*, *105*, pp.7053-7070.

Cloutis, E.A., Craig, M.A., Mustard, J.F., Kruzelecky, R.V., Jamroz, W.R., Scott, A., Bish, D.L., Poulet, F., Bibring, J.P. and King, P.L., 2007. Stability of hydrated minerals on Mars. *Geophysical Research Letters*, *34*(20). https://doi.org/10.1029/2007GL031267

Daubar, I.J. and Kring, D.A., 2001, March. Impact-induced hydrothermal systems: Heat sources and lifetimes. In *Lunar and Planetary Science Conference* (p. 1727).

Daynyak, L.G. and Drits, V.A., 1987. Interpretation of Mössbauer spectra of nontronite, celadonite, and glauconite. *Clays and Clay Minerals*, *35*(5), pp.363-372.

Ding, Z. and Frost, R.L., 2002. Controlled rate thermal analysis of nontronite. *Thermochimica Acta*, *389*(1-2), pp.185-193.

Dos Santos, R., Patel, M., Cuadros, J., Martins, Z., 2016. Influence of Mineralogy on the Preservation of Amino Acids under Simulated Mars Conditions. *Icarus*, *277*, pp. 342–353.

Eggleton, R.A. and Tilley, D.B., 1998. Hisingerite: A ferric kaolin mineral with curved morphology. *Clays and Clay Minerals*, *46*(4), pp.400-413.

Ehlmann, B. L., Mustard, J. F., Fassett, C. I., Schon, S. C., Head III, J. W., Des Marais, D. J., Grant, J. A., & Murchie, S. L., 2008. Clay minerals in delta deposits and organic preservation potential on Mars. *Nature Geoscience*, *1*(6), pp.355–358. https://doi.org/10.1038/ngeo207

Ehlmann, B.L., Mustard, J.F., Swayze, G.A., Clark, R.N., Bishop, J.L., Poulet, F., Des Marais, D.J., Roach, L.H., Milliken, R.E., Wray, J.J. and Barnouin-Jha, O., 2009. Identification of hydrated silicate minerals on Mars using MRO-CRISM: Geologic context near Nili Fossae and implications for aqueous alteration. *Journal of Geophysical Research: Planets*, *114*(E2). https://doi.org/10.1029/2009JE003339

Ehlmann, B. L., Mustard, J. F., Murchie, S. L., Bibring, J. P., Meunier, A., Fraeman, A. A., & Langevin, Y., 2011. Subsurface water and clay mineral formation during the early history of Mars. *Nature*, *479*(7371), pp.53-60.

Ehlmann, B. L., & Mustard, J. F., 2012. An in-situ record of major environmental transitions on early Mars at Northeast Syrtis Major. *Geophysical Research Letters*, *39*(11). https://doi.org/10.1029/2012GL051594.

Ellis, B.G. and Mortland, M.M., 1962. A comparison of two methods of determining heats of reaction by differential thermal analysis. *American Mineralogist: Journal of Earth and Planetary Materials*, *47*(3-4_Part_1), pp.371-378.

Evans, B.W., Kuehner, S.M., Joswiak, D.J. and Cressey, G., 2017. Serpentine, iron-rich phyllosilicates and fayalite produced by hydration and Mg depletion of peridotite, Duluth Complex, Minnesota, USA. *Journal of Petrology*, *58*(3), pp.495-512.

Fairén, A.G., Chevrier, V., Abramov, O., Marzo, G.A., Gavin, P., Davila, A.F., Tornabene, L.L., Bishop, J.L., Roush, T.L., Gross, C. and Kneissl, T., 2010. Noachian and more recent phyllosilicates in impact craters on Mars. *Proceedings of the National Academy of Sciences*, *107*(27), pp.12095-12100.

Farmer, V. C., Krishnamurti, G. S. R., & Huang, P. M., 1991. Synthetic allophane and layer-silicate formation in SiO_2-Al_2O_3-FeO-Fe_2O_3-MgO-H_2O systems at 23°C and 89°C in a calcareous environment. *Clays and Clay Minerals*, *39*(6), pp.561–570. https://doi.org/10.1346/CCMN.1991.039060.

Farmer, V. C., Mchardy, W. J., Elsass, F., & Robert, M., 1994. *hk*-ordering in aluminous nontronite and saponite synthesized near 90°C: Effects of synthesis conditions on nontronite composition and ordering. *Clays and Clay Minerals*, *42*(2), pp.180-186.7.

Fornaro, T., Boosman, A., Brucato, J.R., ten Kate, I.L., Siljeström, S., Poggiali, G., Steele, A. and Hazen, R.M., 2018a. UV irradiation of biomarkers adsorbed on minerals under Martian-like conditions: Hints for life detection on Mars. *Icarus*, *313*, pp.38-60.

Fornaro, T., Steele, A., Brucato, J. R., 2018b. Catalytic/Protective Properties of Martian Minerals and Implications for Possible Origin of Life on Mars. *Life*, *8*, 56, https://doi.org/10.3390/life8040056

French, B.M., 1998. *Traces of catastrophe: A handbook of shock-metamorphic effects in terrestrial meteorite impact structures* (No. LPI-Contrib-954).

Friedlander, L.R., Glotch, T.D., Bish, D.L., Dyar, M.D., Sharp, T.G., Sklute, E.C. and Michalski, J.R., 2015. Structural and spectroscopic changes to natural nontronite induced by experimental impacts between 10 and 40 GPa. *Journal of Geophysical Research: Planets*, *120*(5), pp.888-912.

Gainey, S.R., Hausrath, E.M., Hurowitz, J.A. and Milliken, R.E., 2014. Nontronite dissolution rates and implications for Mars. *Geochimica et Cosmochimica Acta*, *126*, pp.192-211.

Gainey, S.R., Hausrath, E.M., Adcock, C.T., Tschauner, O., Hurowitz, J.A., Ehlmann, B.L., Xiao, Y. and Bartlett, C.L., 2017. Clay mineral formation under oxidized conditions and implications for paleoenvironments and organic preservation on Mars. *Nature Communications*, *8*(1), pp.1-7.

Gainey, S.R., Hausrath, E.M. and Hurowitz, J.A., 2022. Thermodynamic and kinetic analysis of transitions in clay mineral chemistry on Mars. *Icarus*, *372*, p.114733.

Gates, W.P., Slade, P.G., Manceau, A. and Lanson, B., 2002. Site occupancies by iron in nontronites. *Clays and Clay Minerals*, *50*(2), pp.223-239.

Gavin, P. and Chevrier, V., 2010. Thermal alteration of nontronite and montmorillonite: Implications for the martian surface. *Icarus*, *208*(2), pp.721-734.

Gavin, P., Chevrier, V., Ninagawa, K., Gucsik, A. and Hasegawa, S., 2013. Experimental investigation into the effects of meteoritic impacts on the spectral properties of phyllosilicates on Mars. *Journal of Geophysical Research: Planets*, *118*(1), pp.65-80.

Goodman, B.A., Russell, J.D., Fraser, A.R. and Woodhams, F.W.D., 1976. A Mössbauer and IR spectroscopic study of the structure of nontronite. *Clays and Clay Minerals*, *24*(2), pp.53-59.

Goodwin, A., Garwood, R.J. and Tartèse, R., 2022. A review of the "Black Beauty" Martian regolith breccia and its Martian habitability record. *Astrobiology*. https://doi.org/10.1089/ast.2021.0069

Greeley, R. and Spudis, P.D., 1981. Volcanism on mars. *Reviews of Geophysics*, *19*(1), pp.13-41.

Grotzinger, J.P., Crisp, J., Vasavada, A.R. et al., 2012. Mars Science Laboratory Mission and Science Investigation. *Space Science Review 170*, pp. 5–56. https://doi.org/10.1007/s11214-012-9892-2Harder, H., 1976. Nontronite synthesis at low temperatures. *Chemical Geology*, *18*, pp.169-180.

Goudge, T.A., Mustard, J.F., Head, J.W. and Fassett, C.I., 2012. Constraints on the history of open-basin lakes on Mars from the composition and timing of volcanic resurfacing. *Journal of Geophysical Research: Planets*, *117*(E12).

Goudge, T.A., Mustard, J.F., Head, J.W., Fassett, C.I. and Wiseman, S.M., 2015. Assessing the mineralogy of the watershed and fan deposits of the Jezero crater paleolake system, Mars. *Journal of Geophysical Research: Planets*, *120*(4), pp.775-808.

Govindaraju, K. (1994). Compilation of Working Values and Sample Description for 383 Geostandards. Geostandards Newsletter, 18(S1), 1–158. https://doi.org/10.1046/j.1365-2494.1998.53202081.x-i1

Hamilton, V.E. and Christensen, P.R., 2005. Evidence for extensive, olivine-rich bedrock on Mars. *Geology*, *33*(6), pp.433-436.

Harder, H., 1976. Nontronite synthesis at low temperatures. *Chemical Geology*, *18*(3), pp.169-180.

Harder, H., 1978. Synthesis of iron layer silicate minerals under natural conditions. *Clay and Clay Minerals*, *26*(1), pp.65-72.

Hausrath, E.M., Treiman, A.H., Vicenzi, E., Bish, D.L., Blake, D., Sarrazin, P., Hoehler, T., Midtkandal, I., Steele, A. and Brantley, S.L., 2008a. Short- and long-term olivine weathering in Svalbard: Implications for Mars. Astrobiology, 8(6), pp.1079-1092.

Hausrath, E.M., Navarre-Sitchler, A.K., Sak, P.B., Steefel, C.I. and Brantley, S.L., 2008b. Basalt weathering rates on Earth and the duration of liquid water on the plains of Gusev Crater, Mars. Geology, 36(1), pp.67-70.

Heller-Kallai, L. and Rozenson, I., 1980. Dehydroxylation of dioctahedral phyllosilicates. *Clay and Clay Minerals*, *28*(5), pp.355-368.

Hiesinger, H. and Head III, J.W., 2004. The Syrtis Major volcanic province, Mars: Synthesis from Mars global surveyor data. *Journal of Geophysical Research: Planets*, *109*(E1).

Hoefen, T.M., Clark, R.N., Bandfield, J.L., Smith, M.D., Pearl, J.C. and Christensen, P.R., 2003. Discovery of olivine in the Nili Fossae region of Mars. *Science*, *302*(5645), pp.627-630.

Hviid, S.F., Agerkvist, D.P., Olsen, M., Koch, C.B. and Madsen, M.B., 1994. Heated nontronite: possible relations to the magnetic phase in the Martian soil. *Hyperfine Interactions*, *91*(1), pp.529-533.

Ivanova, M. A., Slyutaa, E. N., Grishakinaa, E. A., Dmitrovskiia, A. A., 2020. Geomorphological Analysis of ExoMars Candidate Landing Site Oxia Planum. *Solar System Research*, *54*(1), 1-14.

Joeleht, A., KIRSIMÄE, K., PLADO, J., Versh, E. and Ivanov, B., 2005. Cooling of the Kärdla impact crater: II. Impact and geothermal modeling. *Meteoritics & Planetary Science*, *40*(1), pp.21-33.

Karickhoff, S.W. and Bailey, G.W., 1973. Optical absorption spectra of clay minerals. *Clays and Clay Minerals*, *21*(1), pp.59-70.

Kennedy, M. J., Pevear, D. R., & Hill, R. J., 2002. Mineral surface control of organic carbon in black shale. *Science*, *295*(5555), pp.657–660. https://doi.org/10.1126/science.1066611

Kraus, R.G., Stewart, S.T., Newman, M.G., Milliken, R.E. and Tosca, N.J., 2013. Uncertainties in the shock devolatilization of hydrated minerals: A nontronite case study. *Journal of Geophysical Research: Planets*, *118*(10), pp.2137-2145.

Kremer, C.H., Mustard, J.F. and Bramble, M.S., 2019. A widespread olivine-rich ash deposit on Mars. *Geology*, *47*(7), pp.677-681.

Le Deit, L., Flahaut, J., Quantin, C., Hauber, E., Mège, D., Bourgeois, O., Gurgurewicz, J., Massé, M. and Jaumann, R., 2012. Extensive surface pedogenic alteration of the Martian Noachian crust suggested by plateau phyllosilicates around Valles Marineris. *Journal of Geophysical Research: Planets*, *117*(E11).

Loizeau, D., Mangold, N., Poulet, F., Bibring, J.-P., Gendrin, A., Ansan, V., Gomez, C., Gondet, B., Langevin, Y., Masson, P., & Neukum, G., 2007. Phyllosilicates in the Mawrth Vallis region of Mars. *Journal of Geophysical Research: Planets*, *112*(E8). https://doi.org /10.1029/2006JE002877.

Loizeau, D., Mangold, N., Poulet, F., Ansan, V., Hauber, E., Bibring, J.-P., Gondet, B., Langevin, Y., Masson, P., & Neukum, G., 2010. Stratigraphy in the Mawrth Vallis region through OMEGA, HRSC color imagery and DTM. *Icarus*, *205*(2), pp.396–418. https://doi.org/10.1016/j.icarus.2009.04.018

MacArthur, J. L., Bridges, J. C., Hicks, L. J., Burgess, R., Joy, K. H., Branney, M. J., ... & Ireland, T. R., 2019. Mineralogical constraints on the thermal history of martian regolith breccia Northwest Africa 8114. *Geochimica et Cosmochimica Acta*, *246*, pp. 267-298.

MacKenzie, K.J.D. and Rogers, D.E., 1977. Thermal and Mössbauer studies of iron-containing hydrous silicates: I. nontronite. *Thermochimica Acta*, *18*(2), pp.177-196.

Malin, M. C., & Edgett, K. S., 2000. Sedimentary rocks of early Mars. *Science*, *290*(5498), pp.1927–1937. https://doi.org/10.1126/science.290.5498.1927

Mangold, N., Poulet, F., Mustard, J.F., Bibring, J.P., Gondet, B., Langevin, Y., Ansan, V., Masson, P., Fassett, C. and Head, J.W., 2. coauthors, 2007. Mineralogy of the Nili Fossae region with OMEGA/Mars Express data: 2. Aqueous alteration of the crust. *Journal of Geophysical Research*, *112*. doi:10.1029/2006JE002835Merola, R.B., Fournier, E.D. and McGuire, M.M., 2007. Spectroscopic investigations of Fe^{2+} complexation on nontronite clay. *Langmuir*, *23*(3), pp.1223-1226.

McKeown, N.K., Bishop, J.L., Noe Dobrea, E.Z., Ehlmann, B.L., Parente, M., Mustard, J.F., Murchie, S.L., Swayze, G.A., Bibring, J.P. and Silver, E.A., 2009. Characterization of phyllosilicates observed in the central Mawrth Vallis region, Mars, their potential formational processes, and implications for past climate. *Journal of Geophysical Research: Planets*, *114*(E2).

Melosh, H.J., 1989. Impact cratering: A geologic process. *New York: Oxford University Press; Oxford: Clarendon Press*.

Merola, R.B., Fournier, E.D. and McGuire, M.M., 2007. Spectroscopic investigations of Fe2+ complexation on nontronite clay. *Langmuir*, *23*(3), pp.1223-1226.

Mertzman, S. (2000). K-Ar results from the southern Oregon-northern California Cascade Range. Oregon Geol., 62, 99–122.

Michalski, J.R. and Noe Dobrea, E.Z., 2007. Evidence for a sedimentary origin of clay minerals in the Mawrth Vallis region, Mars. *Geology*, *35*(10), pp.951-954.

Michalski, J.R. and Niles, P.B., 2010. Deep crustal carbonate rocks exposed by meteor impact on Mars. *Nature Geoscience*, *3*(11), pp.751-755.

Michalski, J.R., Glotch, T.D., Friedlander, L.R., Darby Dyar, M., Bish, D.L., Sharp, T.G. and Carter, J., 2017. Shock metamorphism of clay minerals on Mars by meteor impact. *Geophysical Research Letters*, *44*(13), pp.6562-6569.

Milliken, R.E., Egdett, K.S., Swayze, G., Clark. R.N., Thomson, B.J., Anderson, R., and Bell III., J.F., 2009. Clay and sulfate-bearing rocks in a stratigraphic sequence in Gale Crater. *Lunar and Planetary Science Conference XL, 1479* (abstract).

Milliken, R.E., Grotzinger, J.P. and Thomson, B.J., 2010. Paleoclimate of Mars as captured by the stratigraphic record in Gale Crater. *Geophysical Research Letters*, *37*(4). https://doi.org/10.1029/2009GL041870

Milliken, R.E. and Bish, D.L., 2014, March. Distinguishing hisingerite from other clays and its importance for Mars. *In Lunar and Planetary Science Conference No. 1777*, pp.2251.

Morris, R.V., Ming, D.W., Golden, D.C., Graff, T.G. and Achilles, C.N., 2010, January. Evidence for Interlayer Collapse of Nontronite on Mars from Laboratory Visible and Near-IR Reflective Spectra. In *Lunar and Planetary Science Conference* (No. JSC-CN-19546).

Moskowitz, B.M. and Hargraves, R.B., 1984. Magnetic cristobalite (?): A possible new magnetic phase produced by the thermal decomposition of nontronite. *Science*, *225*(4667), pp.1152-1154.

Murchie, S.L., Mustard, J.F., Ehlmann, B.L., Milliken, R.E., Bishop, J.L., McKeown, N.K., Noe Dobrea, E.Z., Seelos, F.P., Buczkowski, D.L., Wiseman, S.M. and Arvidson, R.E., 2009. A synthesis of Martian aqueous mineralogy after 1 Mars year of observations from the Mars Reconnaissance Orbiter. *Journal of Geophysical Research: Planets*, *114*(E2). https://doi.org/10.1029/2009JE003342

Mustard, J.F., Poulet, F., Head, J.W., Mangold, N., Bibring, J.P., Pelkey, S.M., Fassett, C.I., Langevin, Y. and Neukum, G., 2007. Mineralogy of the Nili Fossae region with OMEGA/Mars Express data: 1. Ancient impact melt in the Isidis Basin and implications for the transition from the Noachian to Hesperian. *Journal of Geophysical Research: Planets*, *112*(E8).

Mustard, J.F., Murchie, S.L., Pelkey, S.M., Ehlmann, B.L., Milliken, R.E., Grant, J.A., Bibring, J.P., Poulet, F., Bishop, J., Dobrea, E.N. and Roach, L., 2008. Hydrated silicate minerals on Mars observed by the Mars Reconnaissance Orbiter CRISM instrument. *Nature*, *454*(7202), pp.305-309.

Mustard, J.F., Ehlmann, B.L., Murchie, S.L., Poulet, F., Mangold, N., Head, J.W., Bibring, J.P. and Roach, L.H., 2009. Composition, morphology, and stratigraphy of Noachian crust around the Isidis basin. *Journal of Geophysical Research: Planets*, *114*(E2).

Negron-Mendoza, A., Ramos-Bernal, S. 2004. The Role of Clays in the Origin of Life. In Origins. Cellular Origin, Life in Extreme Habitats and Astrobiology. Seckbach J., Ed., Springer, Dordrecht: Dordrecht, pp 181–194.

Newsom, H.E., 1980. Hydrothermal alteration of impact melt sheets with implications for Mars. *Icarus*, *44*(1), pp.207-216.

Newsom, H.E., Brittelle, G.E., Hibbitts, C.A., Crossey, L.J. and Kudo, A.M., 1996. Impact crater lakes on Mars. *Journal of Geophysical Research: Planets*, *101*(E6), pp.14951-14955.

Noe Dobrea, E.Z., Bishop, J.L., McKeown, N.K., Fu, R., Rossi, C.M., Michalski, J.R., Heinlein, C., Hanus, V., Poulet, F., Mustard, R.J.F. and Murchie, S., 2010. Mineralogy and stratigraphy of phyllosilicate-bearing and dark mantling units in the greater Mawrth Vallis/west Arabia Terra area: Constraints on geological origin. *Journal of Geophysical Research: Planets*, *115*(E7).

Odom, I. E., 1984. Smectite clay minerals: properties and uses. *Philosophical Transactions of the Royal Society of London, A311*(1517), pp.391-409.

Osinski, G.R. and Pierazzo, E., 2013. Impact cratering: Processes and products. *Impact Cratering*, pp.1-20.

Palchik, N.A., Grigorieva, T.N. and Moroz, T.N., 2013. Composition, structure, and properties of iron-rich nontronites of different origins. *Crystallography Reports*, *58*(2), pp.302-307.

Petit, S., Baron, F., & Decarreau, A., 2017. Synthesis of nontronite and other Fe-rich smectites: A critical review. *Clay Minerals*, *52*(4), pp.469–485. https://doi.org/10.1180/claymin.2017.052.4.05.

Pelkey, S.M., Mustard, J.F., Murchie, S., Clancy, R.T., Wolff, M., Smith, M., Milliken, R., Bibring, J.P., Gendrin, A., Poulet, F. and Langevin, Y., 2007. CRISM multispectral summary products: Parameterizing mineral diversity on Mars from reflectance. *Journal of Geophysical Research: Planets*, *112*(E8).

Poch, O., Jaber, M., Stalport, F., Nowak, S., Georgelin, T., Lambert, J.-F., Szopa, C., Coll, P., 2015. Effect of Nontronite Smectite Clay on the Chemical Evolution of Several Organic Molecules under Simulated Martian Surface Ultraviolet Radiation Conditions. *Astrobiology*, *15* (3), 221–237.

Poulet, F., Bibring, J.P., Mustard, J.F., Gendrin, A., Mangold, N., Langevin, Y., Arvidson, R.E., Gondet, B. and Gomez, C., 2005. Phyllosilicates on Mars and implications for early Martian climate. *Nature*, *438*(7068), pp.623-627.

Poulet, F., Gomez, C., Bibring, J.P., Langevin, Y., Gondet, B., Pinet, P., Belluci, G. and Mustard, J., 2007. Martian surface mineralogy from Observatoire pour la Minéralogie, l'Eau, les Glaces et l'Activité on board the Mars Express spacecraft (OMEGA/MEx): Global mineral maps. *Journal of Geophysical Research: Planets*, *112*(E8).

Poulet, F., Mangold, N., Loizeau, D., Bibring, J.-P., Langevin, Y., Michalski, J., & Gondet, B., 2008. Abundance of minerals in the phyllosilicate-rich units on Mars. *Astronomy and Astrophysics*, *487*, pp.L41–L44. https://doi.org/10.1051/0004-6361:200810150

Poulet, F., Carter, J., Bishop, J. L., Loizeau, D., & Murchie, S. M., 2014. Mineral abundances at the final four curiosity study sites and implications for their formation. *Icarus*, *231*, pp.65–76. https://doi.org/10.1016/j.icarus.2013.11.023

Quantin, C., Carter, J., Thollot, P., Broyer, J., Lozach, L., Davis, J., Grindrod, P., Pajola, M., Baratti, E., Rossato, S., Allemand, P., Bultel, B., Leyrat, C., Fernando, J., Ody, A., 2016.

In: Oxia Planum, the Landing Site for ExoMars 2018. Abstract 2863, 47th Lunar and Planetary Science Conference. Lunar and Planetary Institute, Houston, TX.

Ramirez, R. M., Kopparapu, R., Zugger, M. E., Robinson, T. D., Freedman, R., & Kasting, J. F., 2014. Warming early Mars with CO_2 and H_2. *Nature Geoscience, 7*(1), pp.59–63. https://doi.org/10.1038/NGEO2000

Razzell Hollis, J., Fornaro, T., Rapin, W., Wade, J., Vicente-Retortillo, Á., Steele, A., Bhartia, R., Beegle, L. W., 2021. Detection and Degradation of Adenosine Monophosphate in Perchlorate-Spiked Martian Regolith Analogue, by Deep-Ultraviolet Spectroscopy. *Astrobiology*. https://doi.org/10.1089/ast.2020.2362.

Reichen, L.E. and Fahey, J.J., 1962. improved method for the determination of FeO in rocks and minerals including garnet.

Rice, M.S., Bell III, J.F., Godber, A., Wellington, D., Fraeman, A.A., Johnson, J.R., Kinch, K.M., Malin, M.C. and Grotzinger, J.P., 2013, September. Mastcam multispectral imaging results from the Mars Science Laboratory investigation in Yellowknife Bay. In *European Planetary Science Congress* (Vol. 2013, pp. 762).

Salvatore, M. R., et al., 2018. Bulk mineralogy of the NE Syrtis and Jezero crater regions of Mars derived through thermal infrared spectral analyses. *Icarus, 301*, pp. 76-96.

Schon, S. C., Head, J. W., & Fassett, C. I., 2012. An overfilled lacustrine system and progradational delta in Jezero crater, Mars: Implications for Noachian climate. *Planetary and Space Science, 67*(1), pp. 28-45.

Schultz, R.A. and Frey, H.V., 1990. A new survey of multiring impact basins on Mars. *Journal of Geophysical Research: Solid Earth, 95*(B9), pp.14175-14189.

Schwenzer, S., and Kring, D., 2009. Impact-generated hydrothermal systems capable of forming phyllosilicates on Noachian Mars. *Geology 37*(12), 1091-1094.

Schwenzer, S.P., Abramov, O., Allen, C.C., Clifford, S.M., Cockell, C.S., Filiberto, J., Kring, D.A., Lasue, J., McGovern, P.J., Newsom, H.E. and Treiman, A.H., 2012. Puncturing Mars: How impact craters interact with the Martian cryosphere. *Earth and Planetary Science Letters, 325*, pp.9-17.

Schwenzer, S.P. and Kring, D.A., 2013. Alteration minerals in impact-generated hydrothermal systems–Exploring host rock variability. *Icarus, 226*(1), pp.487-496.

Sherman, D.M., 1985. The electronic structures of Fe^{3+} coordination sites in iron oxides: Applications to spectra, bonding, and magnetism. *Physics and Chemistry of Minerals, 12*, pp.161-175.

Sherman, D.M. and Vergo, N., 1988. Optical (diffuse reflectance) and Mössbauer spectroscopic study of nontronite and related Fe-bearing smectites. *American Mineralogist, 73*(11-12), pp.1346-1354.

Sholes, S. F., Smith, M. L., Claire, M. W., Zahnle, K. J., & Catling, D. C., 2017. Anoxic atmospheres of Mars driven by volcanism: Implications for past environment and life. *Icarus, 290*, pp.46–62. https://doi.org/10.1016/j.icarus.2017.02.022

Singer, R.B., 1982. Spectral evidence for the mineralogy of high-albedo soils and dust on Mars. *Journal of Geophysical Research, 87(B12)*, pp.10159-10168.

Tanaka, K.L., Skinner Jr, J.A., Dohm, J.M., Irwin III, R.P., Kolb, E.J., Fortezzo, C.M., Platz, T., Michael, G.G. and Hare, T.M., 2014. Geologic map of Mars.

Tornabene, L.L., Moersch, J.E., McSween Jr, H.Y., Hamilton, V.E., Piatek, J.L. and Christensen, P.R., 2008. Surface and crater-exposed lithologic units of the Isidis Basin as mapped by coanalysis of THEMIS and TES derived data products. *Journal of Geophysical Research: Planets*, *113*(E10).

Tu, V.M., Rampe, E.B., Bristow, T.F., Thorpe, M.T., Clark, J.V., Castle, N., Fraeman, A.A., Edgar, L.A., McAdam, A., Bedford, C. and Achilles, C.N., 2021. A review of the phyllosilicates in Gale Crater as detected by the CheMin instrument on the Mars Science Laboratory, Curiosity rover. *Minerals*, *11*(8), pp.847.

Tutolo, B.M., Evans, B.W. and Kuehner, S.M., 2019. Serpentine-hisingerite solid solution in altered ferroan peridotite and olivine gabbro. *Minerals*, *9*(1), pp.47. https://doi.org/10.3390/min9010047

Varma, R. S., 2002. Clay and clay-supported reagents in organic synthesis. *Tetrahedron*, *58*(7), pp.1235–1255. https://doi.org/10.1016/S0040-4020(01)01216-9

Velde, B., 2014. 9.12—Green Clay Minerals. In H. D. Holland & K. K. Turekian (Eds.), *Treatise on Geochemistry (Second Edition)* (pp. 351–364). Elsevier. https://doi.org/10.1016/B978-0-08-095975-7.00712-9

Wang, X., Li, Y. and Wang, H., 2020. Structural characterization of octahedral sheet in dioctahedral smectites by thermal analysis. *Minerals*, *10*(4), p.347.

Weldon, R.J., Thomas, W.M., Boslough, M.B. and Ahrens, T.J., 1982. Shock-induced color changes in nontronite: Implications for the Martian fines. *Journal of Geophysical Research: Solid Earth*, *87*(B12), pp.10102-10114.

Werner, S.C., 2005. *Major aspects of the chronostratigraphy and geologic evolutionary history of Mars*. Cuvillier Verlag.

Whelan, J.A. and Goldich, S.S., 1961. New data for hisingerite and neotocite. *American Mineralogist: Journal of Earth and Planetary Materials*, *46*(11-12), pp.1412-1423.

Wiens, R.C., Udry, A., Beyssac, O., Quantin-Nataf, C., Mangold, N., Cousin, A., Mandon, L., Bosak, T., Forni, O., Mclennan, S.M. and Sautter, V., 2022. Compositionally and density stratified igneous terrain in Jezero crater, Mars. *Science advances*, *8*(34), p.eabo3399.

Williams, L. B., Canfield, B., Voglesonger, K. M., & Holloway, J. R., 2005. Organic molecules formed in a "primordial womb." *Geology*, *33*(11), pp.913–916. https://doi.org/10.1130/G21751.1

Wilson, M.J., 2013. Smectite clay minerals in: *Sheet Silicates, Rock-Forming Minerals*, vol 3C (Deer, W.A., Howie, R.A., and Zussman, J., editors). The Geological Society, London.

Wray, J.J., Ehlmann, B.L., Squyres, S.W., Mustard, J.F. and Kirk, R.L., 2008. Compositional stratigraphy of clay-bearing layered deposits at Mawrth Vallis, Mars. *Geophysical Research Letters*, *35*(12).

Wray, J.J., Murchie, S.L., Squyres, S.W., Seelos, F.P. and Tornabene, L.L., 2009. Diverse aqueous environments on ancient Mars revealed in the southern highlands. *Geology*, *37*(11), pp.1043-1046.

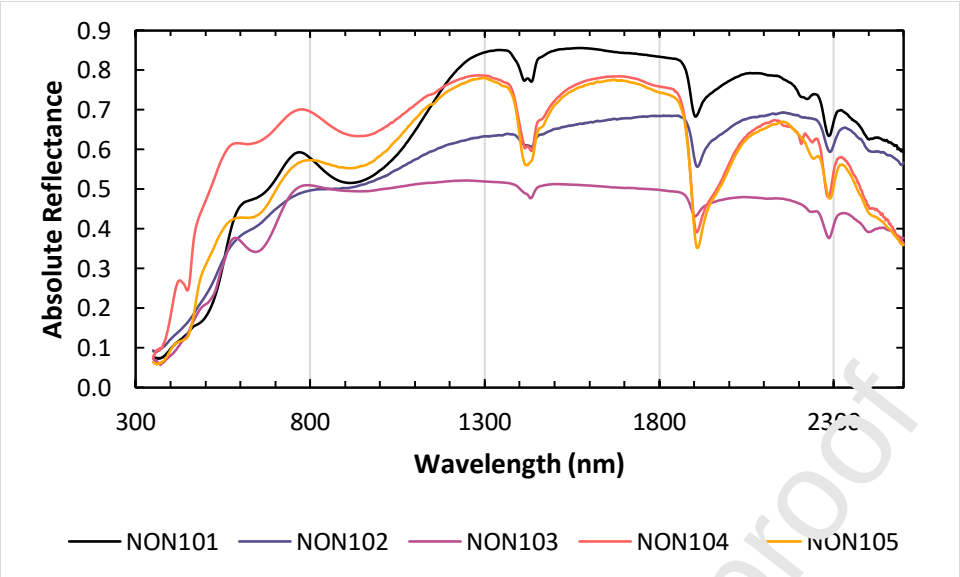

Figure 1a. Reflectance spectra for NON101-105: all <45 µm powders.

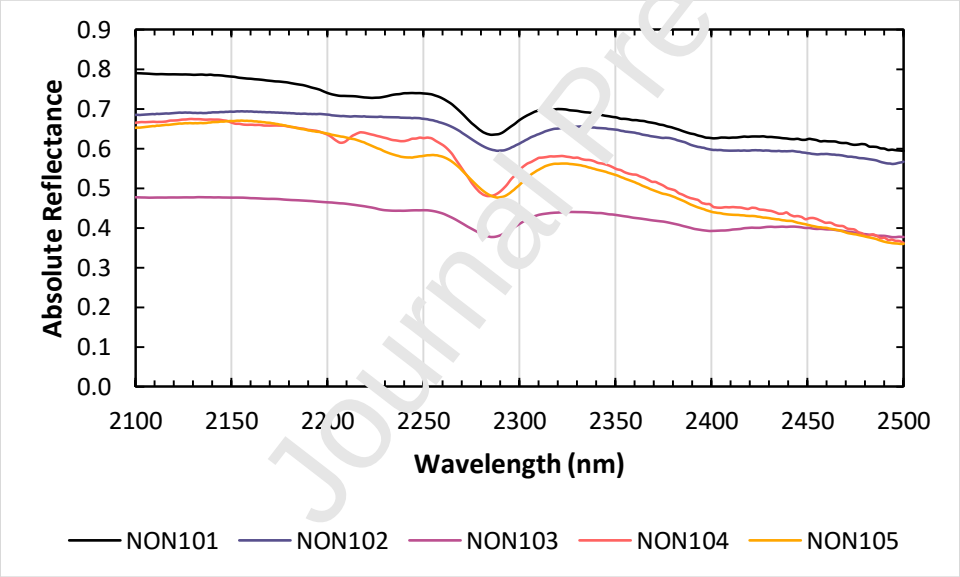

Figure 1b. Same as Figure 1a, showing details in the 2100-2500 nm region.

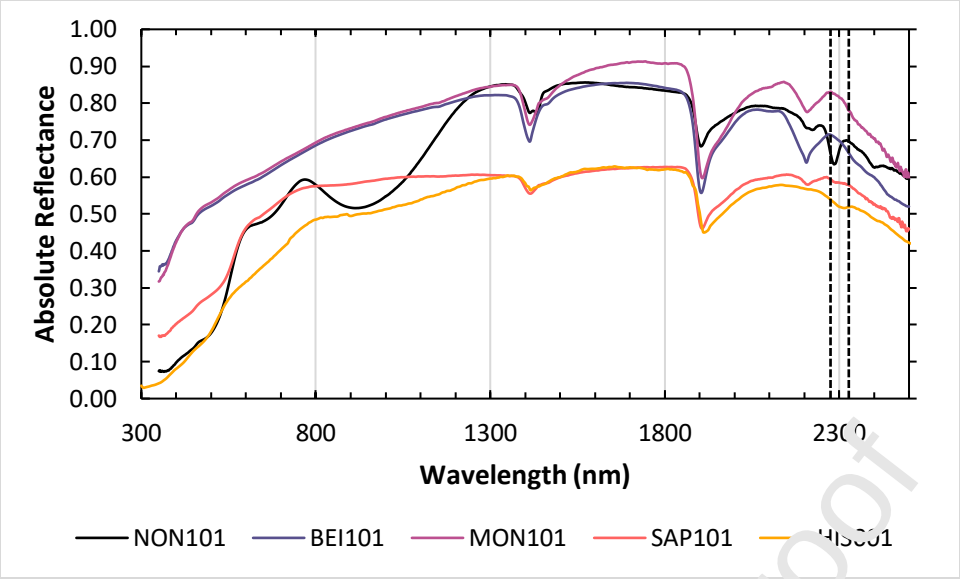

Figure 2a. Reflectance spectra of phyllosilicate clay minerals including the smectite-group minerals nontronite (NON101), beidellite (BEI101), montmorillonite (MON101), saponite (SAP101), and poorly-crystalline hisingerite (HIS001). Dashed lines represent 2280 nm and 2320 nm.

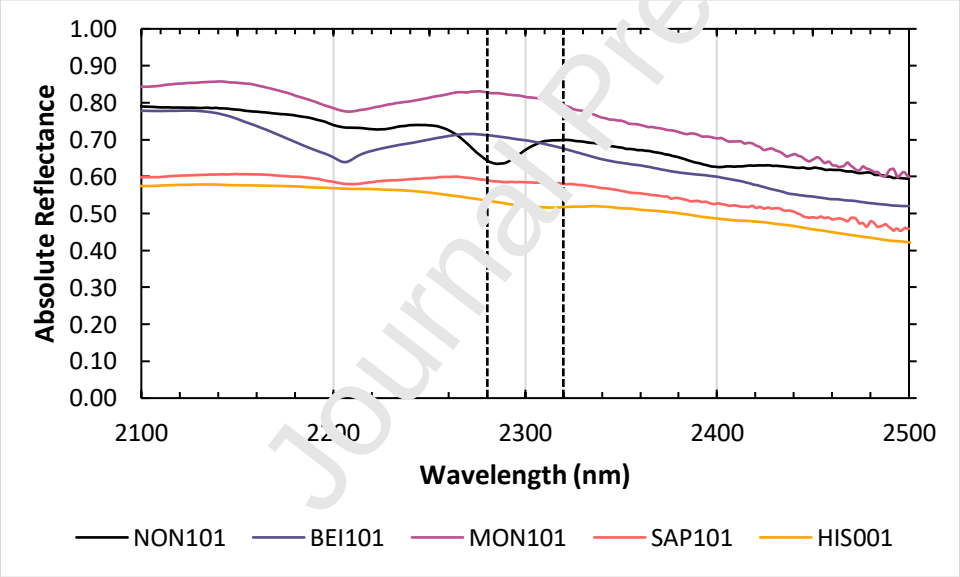

Figure 2b. Same as Figure 2a, showing details in the 2100-2500 nm region. Dashed lines represent 2280 nm and 2320 nm.

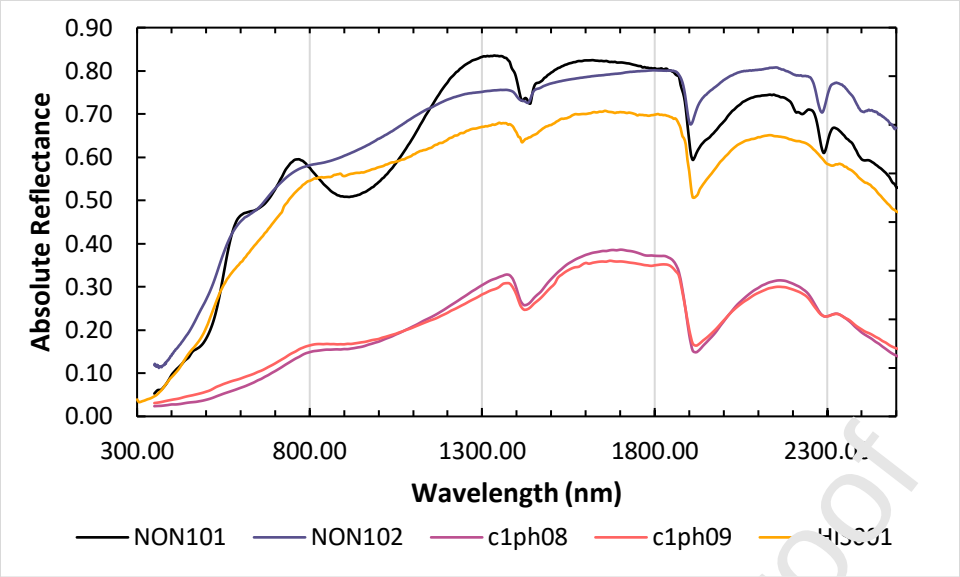

Figure 3. Nontronite (NON101 and NON102) and hisingerite (c1ph08, c1ph09, and HIS001) reflectance spectra (<45 µm grain size for NON101-102 and HIS001, <75 µm grain size for c1ph08 and c1ph09). Spectra collected at RELAB with exception of NON102. C1ph08 and 09 are glassy natural terrestrial hisingerite samples from Beaver Bay, MN, USA (see text for details).

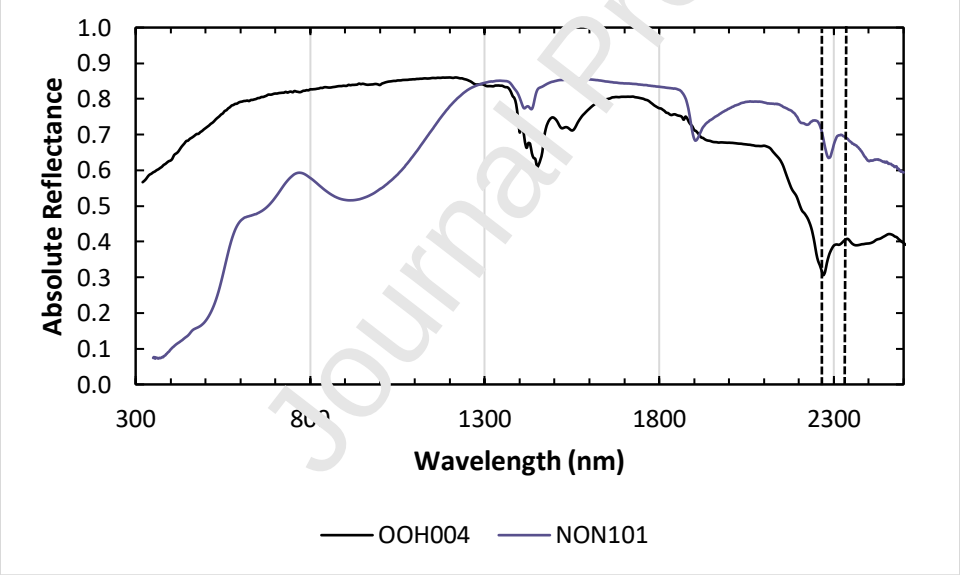

Figure 4. Nontronite (NON101) and gibbsite (OOH001) reflectance spectra (<45 µm grain size); measured at RELAB. Dashed lines represent 2280 nm and 2320 nm.

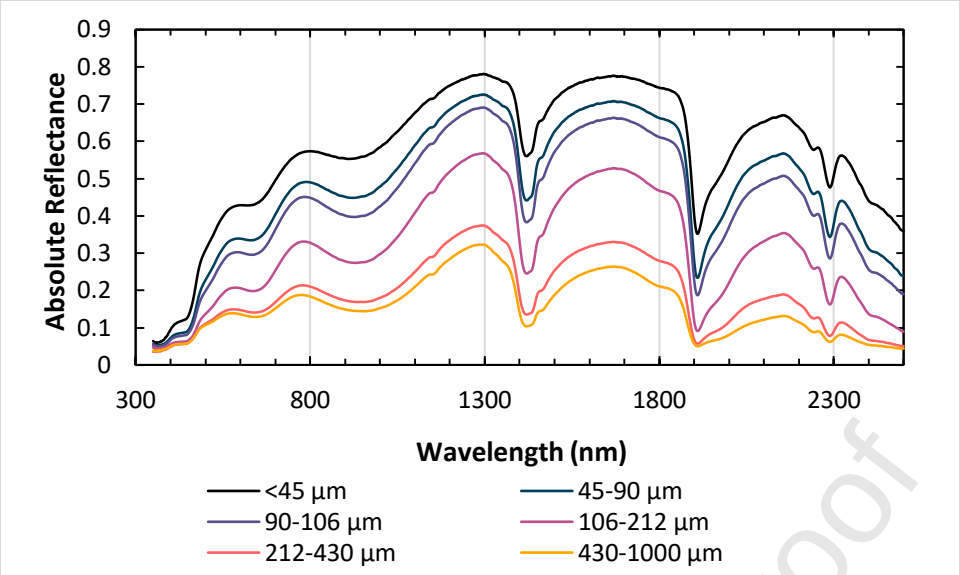

Figure 5. Reflectance spectra of NON105 for different grain size fractions as indicated.

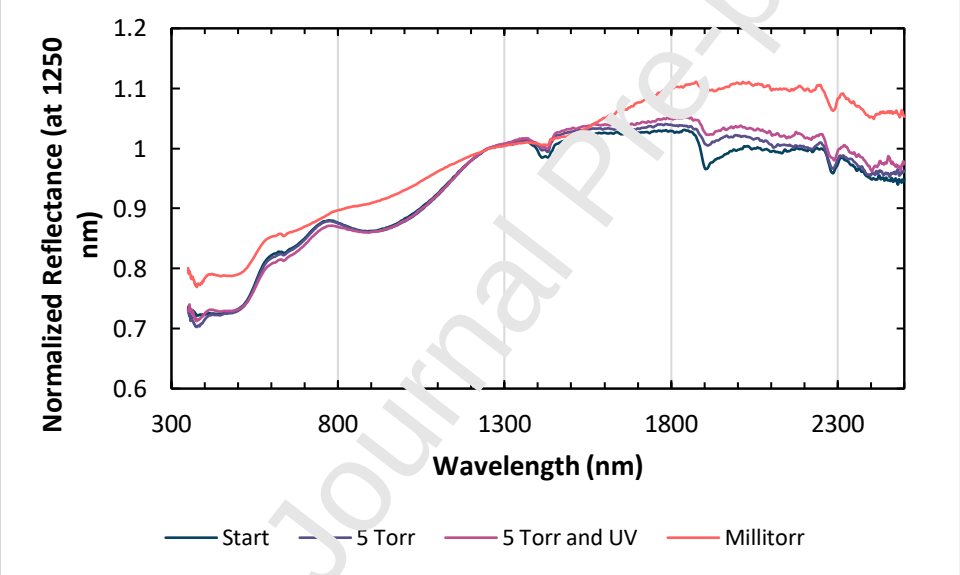

Figure 6. Reflectance spectra of <45 µm NON101 at the start and end of exposure of the sample to 14 days of Mars-like pressures (660 Pa) followed by an additional 9 days at the same pressure plus UV irradiation, followed by 25 days of a few Pa (millitorr) pressures (all in a low-pressure CO_2 atmosphere), measured while in the environment chamber through a sapphire window. See Cloutis et al. (2007) for details.

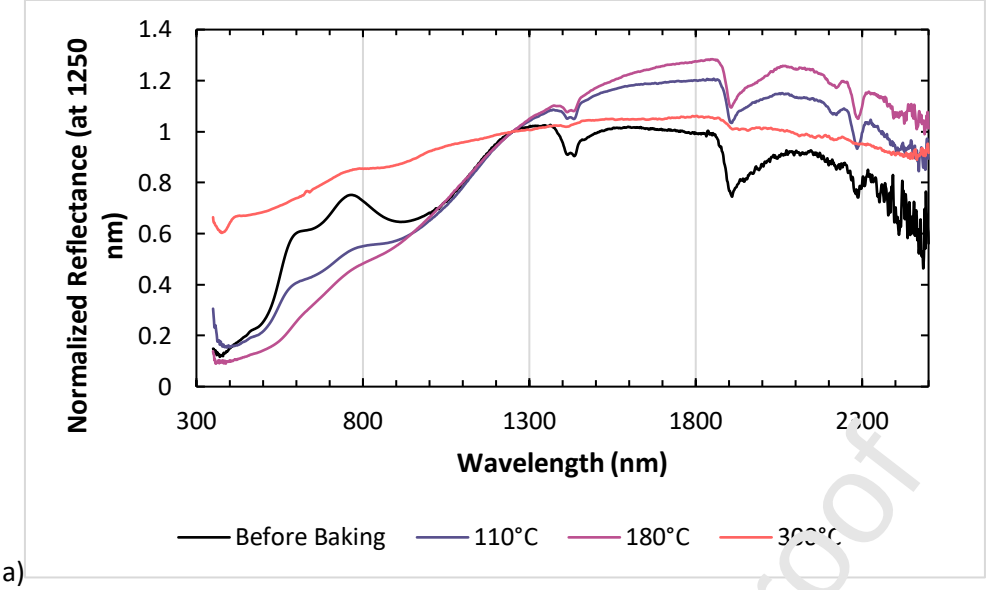

a)

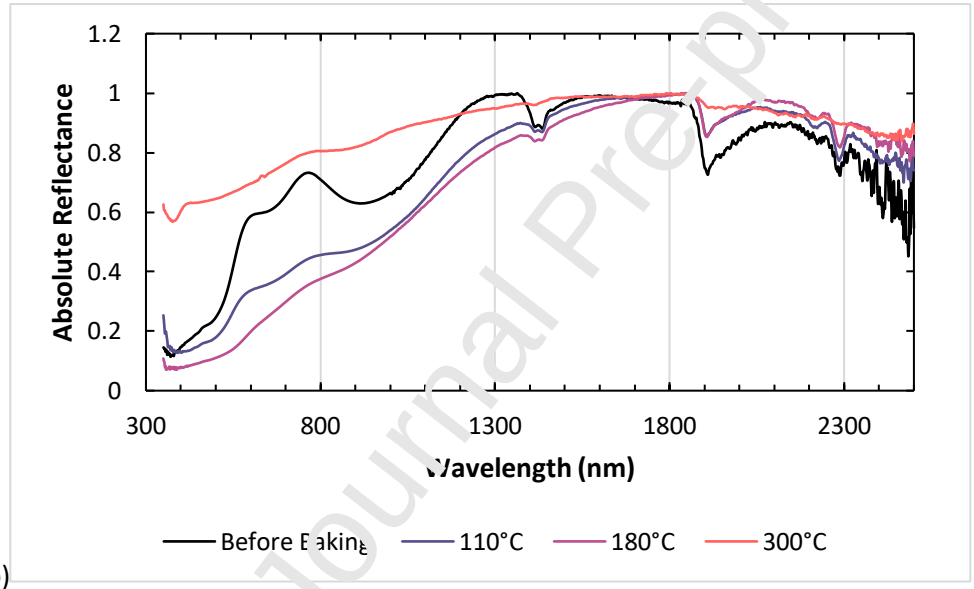

b)

Figure 7. Reflectance spectra of <45 µm powder of NON101 heated at 110, 180 and 300 in a sealed environment chamber (dry CO_2 at 15-75 Torr pressure) for 7 days at each temperature interval; spectra were measured in air after removal from the oven. a) Normalized reflectance at 1250 nm b) Absolute reflectance.

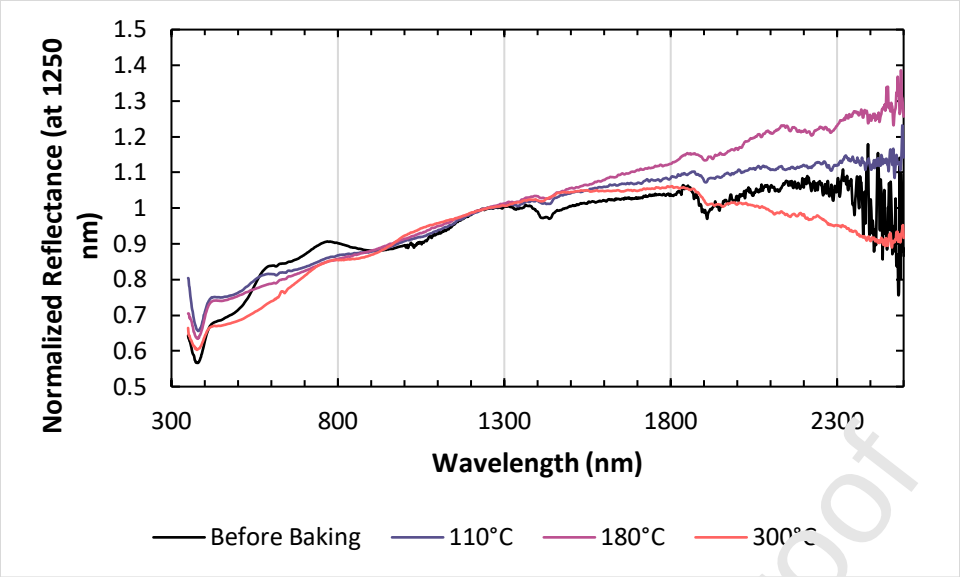

Figure 8. Reflectance spectra of <45 µm powder of NON101 heated at 110, 180 and 300 in a sealed environment chamber (dry CO_2 at 15-75 Torr pressures) for 7 days at each temperature interval; spectra were measured through a sapphire window after removal from the oven.

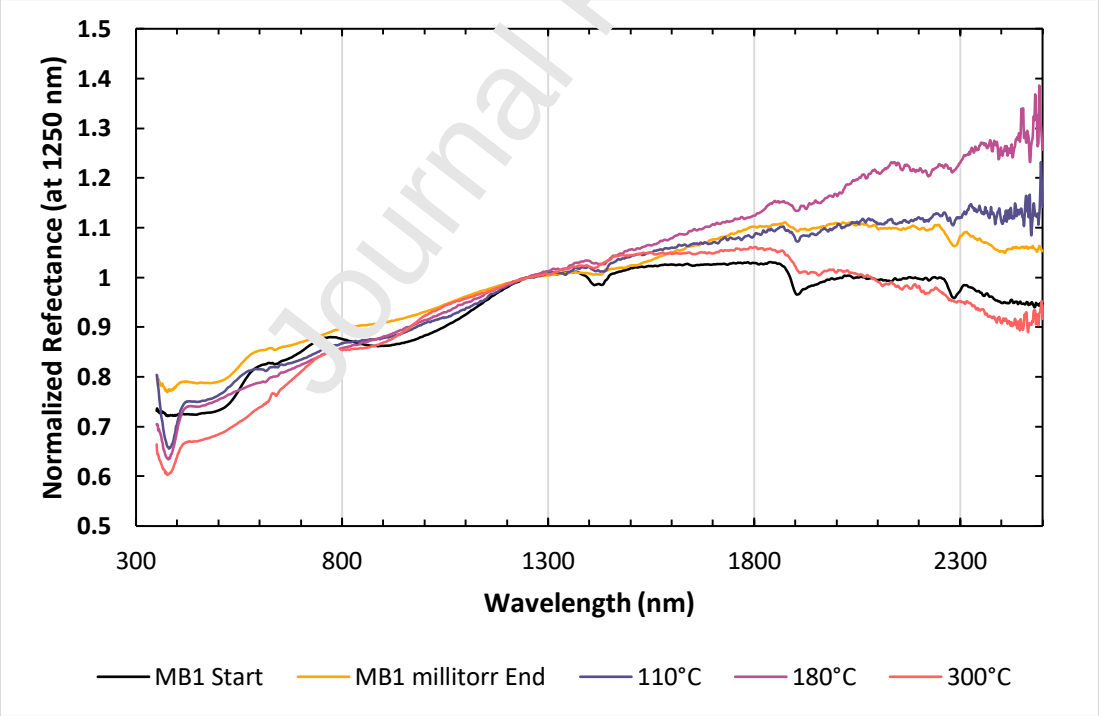

Figure 9. Reflectance spectra of <45 µm powder of NON101 before and after exposure to 660 Pa and few Pa conditions (see Figure 5), along with heating at 100, 180 and 300 °C (see Figures 6 and 7). All spectra were measured through a sapphire window. See text for details.

Table 1. Sources of the samples included in this study and from previous relevant studies.

Nontronite: NON101	Allentown, Lehigh County, PA, USA. Sourced from Minerals Unlimited.
Nontronite: NON102	Hohen Hagen, Germany. Clay Minerals Society Source Clays Repository #NG-1.
Nontronite: NON103	Uley Mine, South Australia, Australia. Clay Minerals Society Source Clays Repository #NAu-2.
Nontronite: NON104	Uley Mine, South Australia, Australia. Clay Minerals Society Source Clays Repository #NAu-1.
Nontronite: NON105	Collected from type locality (road cut) of Clay Minerals Society Source Clays Repository sample SWa-1.
Hisingerite: HIS001	New Pit, Boron, Kern County, California, USA. Sourced from Minerals Unlimited.
Hisingerite: c1ph08	Beaver Bay, MN, USA. glassy natural terrestrial hisingerite, collected from an iron-rich gabbroic bedrock with fayalitic olivine and iron-rich pyroxene. Spectrum taken from the NASA RELAB public database.
Hisingerite: c1ph09	Beaver Bay, MN, USA. glassy natural terrestrial hisingerite, collected from an iron-rich gabbroic bedrock with fayalitic olivine and iron-rich pyroxene. Spectrum taken from the NASA RELAB public database.
Bauxite (gibbsite): OOH001	Guyana (Minerals Unlimited). Sourced from Alcan International.
From previous studies	
Boslough et al. (1980) and Weldon et al. (1982)	Riverside, CA, USA
Cloutis et al. (2007)	NON101
Gavin and Chevrier (2010)	Ca,Al–nontronite fom Cheney, WA, USA (Ward's #49E5108) $(Ca_{0.15}Na_{0.01}K_{0.01})(Fe^{3+}_{1.3}Al_{0.63}Mg_{0.10})(Si_{3.57}Al_{0.45})O_{10}(OH)_2 \bullet nH_2O$
Morris et al. (2010)	PHY07: Pennsylvania, USA, and API33A: Garfield, WA, USA.

Che and Glotch (2012)	Clay Minerals Society Source Clay Repository: SWy-2; NAu-1; NAu-2
Gavin et al. (2013)	Ca,Al–nontronite fom Cheney, WA, USA (Ward's #49E5108) $(Ca_{0.15}Na_{0.01}K_{0.01})(Fe^{3+}_{1:3}Al_{0.63}Mg_{0.10})(S_{i3.57}Al_{0.45})O_{10}(OH)_2 \bullet nH_2O$
Friedlander et al. (2015)	Clay Minerals Society Source Clay Repository: NAu-1
Michalski et al. (2017)	Unknown: "well-characterized sample"

Table 2. Compositions of the five nontronite samples (NON101-105), hisingerite (HIS001), and gibbsite (OOH001) were included in this study. Compositions were determined by a combination of X-ray fluorescence and wet chemistry – see text for details.

Wt. %	*NON101*	*NON102*	*NON103*	*NON104*	*NON105*	*OOH001*	*HIS001*
SiO_2	61.40	55.47	56.08	51.98	54.04	1.83	46.36
Al_2O_3	9.49	9.92	4.89	9.14	8.09	58.56	5.71
TiO_2	0.38	0.21	0.56	0.23	0.46	1.99	0.48
Fe_2O_3[a]	22.08	29.13	34.15	35.20	33.13	N/A	30.53
FeO[b]	0.79	0.48	0.65	0.17	0.14	N/A	0.00
(Fe_2O_3)[c]	*(22.96)*	*(29.66)*	*(34.87)*	*(35.39)*	*(33.29)*	*(0.54)*	*(30.53)*
MgO	1.07	1.16	0.98	1.10	1.60	0.02	9.77
CaO	0.10	0.20	1.79	2.18	2.48	0.05	2.00
Na_2O	0.15	0.02	0.52	0.17	0.61	0.34	3.17
K_2O	3.67	2.32	0.06	0.11	0.02	3.67	0.26
MnO	0.03	0.03	0.01	0.01	0.03	0.003	0.39
P_2O_5	0.51	0.46	0.09	0.02	0.03	0.51	0.08
SO_3	N/A	N/A	0.06	N/A	N/A	N/A	N/A
$TOTAL$[d]	99.76	99.45	99.91	100.33	100.05	99.76	98.75
LOI[e]	8.56	14.46	9.79	21.92	23.11	8.56	14.63
ppm							
Sr	40	12	112	59	32	40	320
Zr	445	117	70	<2	26	0.12	340
V	70	24	223	124	196	0.011	75
Cr	15	<2	63	<2	<2	N/A	640
Ni	N/A	N/A	13	N/A	N/A	0.0013	400
Co	N/A	N/A	<1	N/A	N/A	N/A	50
Rb	N/A	22	N/A	<2	<2	N/A	<2
Ba	N/A	341	N/A	43	49	N/A	N/A
Source	Mertzman	Mertzman	Mertzman	Mertzman	Mertzman	Mertzman	Mertzman
Analysis	XRF/WC	XRF/WC	XRF/WC	XRF/WC	XRF/WC	XRF/WC	XRF/WC

[a] Fe_2O_3 determined as the difference between total Fe (from X-ray fluorescence analysis) and FeO as determined by wet chemistry (see text for details).

[b] FeO determined by wet chemistry (see text for details).

[c] all Fe reported as Fe_2O_3.

[d] total expressed on a volatile (LOI)-free basis and with all Fe reported as Fe_2O_3.

[e] LOI: loss on ignition = % weight loss after heating sample in air for 60-90 minutes.

[f] - SCMR: Source Clay Minerals Repository database.

Abbreviations: Mertzman: analysis done at Franklin and Marshall College – see text for details. XRF: X-ray fluorescence. WC: wet chemistry.

N/A table entries indicate analysis for this element was not performed.

Table 3. Phases identified in the samples included in this study by X-ray diffractometry

Sample ID	*Phases identified*
NON101	Nontronite, minor quartz
NON102	Nontronite, trace quartz
NON103	Nontronite, amorphous component, trace talc
NON104	Nontronite, amorphous component, trace goethite
NON105	Nontronite, amorphous component
HIS001	Hisingerite, amorphous component
OOH001	Gibbsite

Table 4. Selected absorption band centers from continuum-removed spectra for nontronite, hisingerite, and gibbsite, and mimima (no continuum removal).

	Absorption band center position (nm)			
Mineral and sample ID	**1400 nm region**	**1900 nm region**	**2200 nm region**	**2300 nm region**
Nontronite: NON101	1415, 1440	1910	2290	2400
Nontronite: NON102	1415, 1432	1904	2285	2397
Nontronite: NON103	1415, 1432	1903	2286	2399
Nontronite: NON104	1415, 1430	1905	2283	2395
Nontronite: NON105	1419, 1435	1909	2288	2399
Hisingerite: HIS001	1415	1910	2300	N/A
Hisingerite: c1ph08	1420	1920	2290	N/A
Hisingerite: c1ph09	1430	1920	2290	N/A
Gibbsite: OOH001	1405,1425,1450	N/A	2270	2310, 2365

*Band centers were identified with the continuum-removal method outlined.

*Spectral band anchors include 1360 and 1520 nm, 1840 and 2050 nm, 2235 and 2350 nm, 2350 and 2420 nm. Gibbsite anchors in addition to above at 2300 and 2340, 2340 and 2380 nm.

	Absorption band minima position (no continuum removal) (nm)			
Mineral and sample ID	**1400 nm region**	**1900 nm region**	**2200 nm region**	**2300 nm region**
Nontronite: NON101	1415, 1440	1910	2285	2410
Nontronite: NON102	1415, 1432	1904	2289	2407
Nontronite: NON103	1415, 1434	1903	2286	2399
Nontronite: NON104	1415, 1433	1905	2284	2420
Nontronite: NON105	1420, 1435	1910	2289	2420
Hisingerite: HIS001	1415	1915	2315	N/A
Hisingerite: c1ph08	1420	1920	2290	N/A
Hisingerite: c1ph09	1420	1920	2300	N/A
Gibbsite: OOH001	1405,1425,1450	N/A	2270	2315, 2360

N/A: no absorption band present.

Table 5. Depths of absorption bands (in percent), and wavelength position of ~750 nm local reflectance maximum in nontronite spectra from this and previous studies

Source	**Sample**	**650 nm**	**~780 nm**	**900 nm**	**1400 nm**	**1900 nm**	**2280 nm**	**2400 nm**

		region band[a]	refl. max.[b]	region band[c]	region band[d]	region band[e]	region band[f]	region band[g]
Cloutis et al. (2007):	Ambient	2	760 nm	4	4	6	3	2
Low-pressure CO_2	End of 5 Tor	2	770 nm	3	3	3	3	2
	End of milliTorr	<1	nb	1	2	2	3	2
Gavin and Chevrier (2010): heating[h]	Untreated	na	na	na	100	100	100	nd
	400°C	na	na	na	8	30	4	nd
	475°C	na	na	na	6	18	4	nd
	630°C	na	na	na	5	140	27	0
	725°C	na	na	na	0	0	1	0
	800°C	na	na	na	0	0	2	0
	900°C	na	na	na	0	0	0	0
	975°C	na	na	na	0	0	0	0
	1130°C	na	na	na	0	0	0	0
Morris et al. (2010): heating[i]	PHY07: Air, 25°C	>0	800 nm	>0	>0	>0	>0	>0
	25°C, 410 hours, N_2	>0	780 nm	>0	>0	>0	>0	>0
	50°C, 168 hours, N_2	>0	780 nm	>0	>0	>0	>0	>0
	105°C, 46 hours, N_2	>0	np	>0	>0	>0	>0	>0

	105°C, 451 hours, N_2	0	np	0	>0	>0	>0	>0
	105°C, 1004 hours, N_2	0	np	0	>0	>0	>0	>0
	210°C, 89 hours, N_2	0	np	0	>0	0	>0	>0
	API-33A:							
	Air, 25°C	>0	780 nm	>0	>0	>0	>0	>0
	25°C, 263 hours, N_2	>0	780 nm	>0	>0	>0	>0	>0
	105°C, 142 hours, N_2	>0	780 nm	>0	>0	>0	>0	>0
	105°C, 369 hours, N_2	>0	np	>0	>0	>0	>0	>0
	105°C, 1206 hours, N_2	0	np	0	>0	>0	>0	>0
	210°C, 120 hours, N_2	0	np	0	>0	>0	>0	>0
Che and Glotch (2012): heating	NAu-1:							
	Unheated	na	na	na	16	27	17	6
	100°C	na	na	na	24	49	30	10

	200°C	na	na	na	21	18	28	9
	300°C	na	na	na	14	16	20	6
	400°C	na	na	na	3	12	6	3
	500°C	na	na	na	0	10	4	2
	600°C	na	na	na	0	6	2	1
	700°C	na	na	na	0	1	1	0
	800°C	na	na	na	0	0	0	0
	900°C	na	na	na	0	1	0	0
	NAu-2:							
	Unheated	na	na	na	34	18	44	17
	100°C	na	na	na	35	18	43	18
	200°C	na	na	na	25	15	46	18
	300°C	na	na	na	29	7	42	15
	400°C	na	na	na	2	11	7	10
	500°C	na	na	na	0	13	2	6
	600°C	na	na	na	0	15	0	9
	700°C	na	na	na	0	1	0	0
	800°C	na	na	na	0	0	0	0
	900°C	na	na	na	0	0	0	0
Gavin et al. (2013): shock[h]	Unshocked	na	na	na	>0	>0	>0	>0
	3.27 km/s	na	na	na	>0	>0	>0	>0
Friedlander et al. (2015): shock	Pre-impact	6	760 nm	23	38	59	30	12
	10.2 GPa	6	790 nm	18	26	47	21	10
	19.7 GPa	0	790 nm	8	16	36	11	3
	25.2 GPa	0	780 nm	15	14	37	6	1
	30.6 GPa	0	780 nm	22	14	35	6	1
	34.6 GPa	0	790 nm	10	7	21	1	0
	39.1 GPa	0	780 nm	14	7	25	1	0
Michalski et al. (2017): shock	Unshocked	na	na	na	>0	>0	26	>0
	10 GPa	na	na	na	>0	>0	20	>0
	20 GPa	na	na	na	>0	>0	12	0

	25 GPa	na	na	na	>0	>0	2	0
	30 GPa	na	na	na	>0	>0	6	0
	35 GPa	na	na	na	>0	>0	0	0
	40 GPa	na	na	na	>0	>0	1	0
This study: grain size	NON105:							
	<45 µm	6	770 nm	23	10	17	12	3
	45-90 µm	13	780 nm	21	38	64	24	11
	90-106 µm	18	780 nm	24	44	70	27	15
	106-212 µm	22	780 nm	35	56	80	34	21
	212-430 µm	20	780 nm	39	62	78	34	22
	430-1000 µm	19	780 nm	40	66	76	29	19
This study: heating	Through sapphire window:							
	Ambient T°	2	780 nm	5	4	6	3	2
	110° C	1	np	2	2	2	2	2
	180° C	1	np	1	2	2	2	2
	300° C	0	np	3	1	3	1	2
	In air (no window):							
	Ambient T°	6	780 nm	23	11	24	12	15
	110° C	3	np	15	6	14	12	5
	180° C	0	np	10	4	14	10	4
	300° C	0	np	9	3	7	2	2
This study: different	NON101	6	770 nm	23	10	17	12	3
	NON102	3	np	3	5	16	10	4

nontronites (all <45 µm)	NON103	18	780 nm	4	7	12	15	5
	NON104	5	780 nm	13	24	46	20	8
	NON105	8	780 nm	14	28	51	19	7

Notes:

Band depths calculated as 1-Rb/Rc, where Rb is reflectance at the continuum-removed band center, Rc is reflectance of the continuum at the same wavelength as Rb. Values taken to the nearest percent.

Abbreviations: na = wavelength range not covered; nb = no band; nd = relevant data not available; np = no peak present.

[a] Continuum located at ~550 to ~750 nm

[b] Peak wavelength at point of maximum reflectance in the 780 nm region, if distinct peak is present, to closest 10 nm.

[c] Continuum located at ~750 to ~1200 nm

[d] Continuum located at ~1300 to ~1450 nm

[e] Continuum located at ~1850 to ~2100 nm

[f] Continuum located at ~2250 and 2360 nm

[g] Continuum located at ~2350 to ~2450 nm

[h] Published spectra used. Spectra were offset for clarity, so absolute band depths not known. Band depth values are relative to the unheated sample, for which normalized band depth values of one (100%) were assigned.

[i] Published spectra used. Spectra were offset for clarity, so absolute band depths not known.

Table 6. C-TAPE and RELAB database spectral search of minerals with ~2280 and 2320 nm absorption band.

Sample type	Sample ID	XRD phases identified	Fe2O3 (wt.%)	FeO (wt. %)	Fe2O3T	2280 nm	2320 nm	Notes
					(all Fe reported as Fe2O3)	band depth (%)	band depth (%)	
Allophane	ALL001	Allophane + amorphous	0.15	0	0.15	0	0	
Beidellite	BEI101	Beidellite, + others	5.24	0.18	5.44	0	0	Smectite
	BEI102	Beidellite + amorphous			2.05	0	0	Smectite
Berthierine	BER101	Berthierine			13.46	shoulder	2	Fe-serpentine
	BER102	Berthierine + amorphous	30.59	20.41	53.27	shoulder	1	Fe-serpentine; band at 2340 nm
Celadonite	CEL101	Celadonite	18.19	3.57	22.16	0	8	Fe mica; band at 2300 nm
	CEL102	Celadonite; feldspar	9	1.25	10.39	0	3	Fe mica; band at 2300 nm
Chamosite	CHM101	Chamosite?, feldspar	9.62	4.81	14.41	0	0	Fe-chlorite
	CHM102	Chamosite	25.92	29.09	58.25	shoulder	4	Fe-chlorite
	CHM103	Chamosite, albite, quartz	2.87	1.91	4.94	1 (at 2250 nm)	2	Fe-chlorite
Clinochlore (chlorite)	CLI101	Clinochlore	4.23	5.96	10.85	2	10	
	CLI102	Unknown	11.49	4.84	16.87	3	8	
	CLI103	Clinochlore	5.37	24.45	32.54	3 (at 2270 nm)	10 (at 2340 nm)	
Cronstedtite	CRO101	Cronstedtite	63.51	15.96	81.25	0	1	Fe-serpentine
	CRO102	Cronstedtite	52.79	26.79	82.56	0	3	Fe-serpentine
Glauconite	GLA101	Siderite, goethite	35.06	15.19	51.94	0	1	Fe-mica
	GLA102	Siderite quartz; + others	36.99	10.16	47.15	0	2 (at 2300 nm)	Fe-mica
	GLA103	Glauconite, quartz	16.06	1.51	17.74	shoulder maybe	4	Fe-mica

	GLA104	Glauconite, mica	22.65	2.06	24.94	shoulder	8	Fe-mica
	PIG315	Glauconite + amorphous component				0	3	Fe-mica
	PIG317	Gypsum + other minor phases				0	0	Fe-mica
	PIG325	Glauconite				0	3	Fe-mica
Greenalite	GRE001	Greenalite	25.05	36.43	65.34	0	1 (at 2350 nm)	Fe-serpentine
	GRE002	Hematite, chlorite, muscovite	29	10.62	40.8	0	1	Fe-serpentine
Gyrolite	GYR002	Unknown				shoulder	3	
Halloysite	HAL001	Halloysite + amorphous	0.44	0	0.44	0	1	Serpentine group
Hectorite	HEC101	Hectorite, calcite, beidellite				0	11 (at 2310 nm)	Poorly crystalline
	HEC102	N/A				shoulder	7	
Hisingerite	HIS001	Hisingerite + amorphous	30.53	0	30.53	shoulder	2	Poorly crystalline Fe clay
Iddinsite	IDD001	Forsterite, enstatite, amphibole	3.47	5.61	9.7	0	1	Fe clay
Illite	ILL101	Illite	2.87	2.11	4.98	0	3	Smectite
	ILL102	Illite	4.44	1.31	5.9	0	4	Smectite
	ILS103	Illite	1.49	0.1	1.6	0	0	Smectite
	ILS104	Illite	2.19	0.48	2.72	0	0	Smectite
	ILL105	N/A	5.15	1.43	6.74	0	4 (at 2340 nm)	Smectite
Kaolinite	KAO101	Kaolinite	0.36	0.32	0.72	0	3	Kaolinite-serpentine group
	KAO102	Kaolinite	0.08	0.41	0.54	0	2	Kaolinite-serpentine group
	KAO103	Kaolinite	0.26	0.02	0.28	0	0	Kaolinite-serpentine group

	KAO 104	Kaolinite	0.62	0.48	1.15	0	0	Kaolinite-serpentine group
Laponite	LAP0 01	N/A				1	15 (at 2310 nm)	Synthetic hectorite clay
Lepidolite	LEP1 01	Mica	19.43	8.61	29	0	2	Fe mica
Minnesotaite	MIN 001	Minnesotaite, quartz, siderite	11.78	27.35	42.18	0	1	Fe talc
	MIN 002	Greenalite + others	5.12	30.37	37.78	0	1	Fe talc
	MIN 003	Quartz, hematite, chlorite	26.7	9.75	37.54	1 (at 22[illegible] nm)	1 (at 2370 nm)	Fe talc
Montmorillonite	MO N10 1	Montmorillonite	5.65	0.26	5.94	0	0	Smectite
	MO N10 2	Montmorillonite	0.21	4.05	4.71	0	0	Smectite
	MO N10 3	Montmorillonite + amorphous	5.19	0	5.19	0	0	Smectite
Neotocite	NEO 101	Quartz, amorphous component	0.28	0	0.28	0	5 (at 2360 nm)	Amorphous clay
	NEO 102	N/A				0	7 (at 2360 nm)	Amorphous clay
Nontronite	NON 101	Nontronite, quartz	22.08	0.79	22.96	9	0	Fe smectite
	NON 102	Nontronite, trace quartz	29.13	0.48	29.66	7	0	Fe smectite
	NON 103	Nontronite, amorphous, trace talc	34.15	0.65	34.87	5	0	Fe smectite
	NON 104	Nontronite, amorphous, goethite	35.2	0.17	35.39	12	0	Fe smectite
	NON 105	Nontronite, amorphous	33.13	0.14	33.29	8	0	Fe smectite
Palygorskite	PLY1 01	quartz; calcite	1.16	0	1.16	0	0	Palygorskite group phyllosilicate
	PLY1 02	N/A				0	0	Palygorskite group phyllosilicate
Saponite	SAP1 01	Saponite, feldspar	7.29	0.39	7.72	0	0	Smectite
	SAP1 02	Saponite amphibole	0.42	0.54	0.96	shoulder	18	Smectite

	SAP103	Saponite	14.25	3.94	18.63		5	Smectite
	SAP104	N/A	1.55	1.06		shoulder	20	Smectite
	SAP105	Saponite + others	1.86	0.08	1.95	shoulder	8	Smectite
Sepiolite	SEP101	Sepiolite, calcite	1.41	0		0	6	Sepiolite group
	SEP102	N/A				shoulder	9	Sepiolite group
	SEP103	Sepiolite + other phases				0	4	Sepiolite group
Serpentine	SRP101	Serpentine	2.05	1.36	3.56	shoulder	8	Serpentine group
	SRP102	Serpentine, quartz	2.39	0.29	2.71	shoulder	5	Serpentine group
	SRP104	Serpentine	10.11	1.34	11.6	shoulder	6	Serpentine group
	SRP105	Serpentine	0.71	1.34	2.2	2	20	Serpentine group
	SRP106	Serpentine, magnetite	7.28	1.6	9.06	shoulder	4	Serpentine group
	SRP107	Serpentine, augite	5.66	3.73	9.78	shoulder	3	Serpentine group
	SRP108	Serpentine, augite	9.18	3	12.51	shoulder	4	Serpentine group
	SRP109	Serpentine	4.64	3.7	8.34	shoulder	8	Serpentine group
	SRP110	Serpentine	6.51	2.37	9.14	shoulder	7	Serpentine group
	SRP111	Serpentine	4.88	2.72	7.9	shoulder	6	Serpentine group
	SRP112	Serpentine	5.27	2.87	8.46	shoulder	6	Serpentine group
	SRP113	Serpentine	10.1	0.25	10.38	shoulder	7	Serpentine group
	SRP114	Serpentine	6.76	1.08	7.96	shoulder	8	Serpentine group
	SRP115	Serpentine, magnesite	6.7	2.63	9.62	shoulder	5	Serpentine group
	SRP116	Serpentine, forsterite	3.71	5.51	9.83	shoulder	5	Serpentine group
	SRP117	Serpentine	6.8	2.51	9.59	shoulder	5	Serpentine group
	SRP118	Serpentine	3.23	0.58	3.87	shoulder	11	Serpentine group
	SRP119	Serpentine	3.04	1.78	5.02	1	8	Serpentine group
	SRP120	Serpentine	5.64	3.19	9.19	1	10	Serpentine group

	SRP121	Serpentine, chromite	7.32	2.29	9.86	shoulder	2	Serpentine group
	SRP122	Serpentine, + others	7.3	2.26	9.81	shoulder	5	Serpentine group
	SRP123	Serpentine,chromite	7.09	2.85	10.26	shoulder	4	Serpentine group
Talc	TAL001	Talc	0.55	0.43	10.3	23	30	Talc group
	TAL002	Talc				5	15	Talc group
Tochilinite	TOC101	Serpentine			7.21	1	9	
Vermiculite	VER101	Unknown	18.8	0.79	19.68	0	5	Smectite
	VER102	Unknown	9.14	0.99	10.24	0	5	Smectite
	VER103	Biotite/phlogopite	4.52	5.02	10.1	0	7	Smectite
Amphibole	AMP106	N/A	7.67	0	7.67	shoulder	8	
Hydroxides	OOH001	Gibbsite			0.54	14 (at 2270 nm)	2	Gibbsite-rich bauxite
	OOH002	Gibbsite			7.55	11 (at 2270 nm)	1	Gibbsite-rich bauxite
	OOH003	Goethite	96.17	0.43		0	0	
	OOH004	Gibbsite			0.08	14 (at 2270 nm)	1	
	OOH005	Boehmite, goethite			16	1 (at 2270 nm)	3	
	OOH006	Manganite			0.03	0	0	
	OOH007	Diaspore			0.13	shoulder	3	
	OOH008	Diaspore			0.27	0	0	
	OOH009	Diaspore			1.15	0	0	
	OOH010	Diaspore+boehmite, hematite			18.71	1	0	
	OOH011	Diaspore			0.12	0	0	
	OOH012	Diaspore			0.62	0	0	
	OOH013	Diaspore			0.49	0	0	

	OOH 022	Brucite				2 (at 2270 nm)	15	Brucite
	OOH 032	N/A			0.22	1 (at 2270 nm)	10	Brucite
	OOH 034	N/A			0.3	3	15	Brucite
	OOH 035	Goethite				0	0	Goethite
Fe oxyhydroxides	Ferrihydrite					0	0	RELAB archive - 1 spectrum
	Goethite					0	0	RELAB archive - 1 spectrum
	Maghemite					0	0	RELAB archive - 4 spectra
	Lepidocrocite					0	0	RELAB archive - 4 spectra
	Schwertmannite					0	0	RELAB archive - 3 spectra
	Ferrihydrite					0	0	RELAB archive - 2 spectra
	Akaganeite					0	2	RELAB archive - 1 spectrum
	Ferroxyhyte					0	0	RELAB archive - 1 spectrum

Notes:
Shoulder: inflection point present in spectrum, band depth is <1%
2280 nm band: band depth measured relative to a straight line continuum between ~2250 and ~2300 nm
2320 band: band depth measured relative to a straight line continuum between ~2270 and 2360 nm
N/A: not analyzed.

Table 7. Summary of previous relevant studies and this study.

Source	Experimental conditions	Spectral results/findings	Notes
Boslough et al. (1980) and Weldon et al. (1982)	• Shock experiments; 18-30 GPa • <63 µm nontronite powder, pressed into cylinder • 400-2500 nm absorption spectra • Shock experiments conducted in ambient air. • Samples heated to 150°C in dry N_2 prior to spectral measurements • Samples also analyzed by XRD, Mossbauer spectroscopy and optical microscopy.	• Color change from green to brown • Absorbance increases • Reduction in 1400 and 1900 nm hydration and 2320 nm FeOH band depths	• Some bound water lost due to shock-induced heating • Decrease in lattice constant along c-axis • Change in coordination of Fe^{3+}
Weldon et al. (1982)	• Nontronite heated in air and reducing environment to 350° and 550°C for 30 minute intervals • Shocked between 180 and 300 kbar	• Samples heated in reducing environment became darker faster than they became redder • Samples became redder and darker	• Partial dehydroxylation and change in octahedral site coordination
Cloutis et al. (2007)	• <45 µm nontronite powder (NON101) • 350-2500 nm wavelength ranges • 5 Torr (660 Pa) CO_2 for 14 days, followed by additional 7 days with UV irradiation, followed by 25 days at ~10 milliTorr (few Pa) • Sample analyzed by XRD, XRF, and wet chemistry	• 650 nm FeOH band persists at Mars pressures; disappears at milliTorr pressures • 750 nm peak shifts to slightly longer wavelength, becomes shoulder at milliTorr pressures • Reduction in 1400 and 1900 nm hydration band depths • ~2280 and 2400 nm FeOH bands unaffected • Spectrum below ~1400 nm becomes flatter at milliTorr pressure	•
Gavin and Chevrier (2010)	• <63 µm nontronite powder • 1000-2500 nm and 1.4-28.6 µm wavelength ranges • 395°-1130°C heating for 4-24 hours under air or continuous CO_2. • Sample analyzed by XRD	• Reduction in 1400 and 1900 nm hydration band depths, disappear at different temperatures and for different samples; generally above 500°C. • 2280 nm FeOH band disappears by 395° C.	• Interlayer water lost above ~400°C • Layered structure lost by ~475°C. • Intermediate anhydrous phase forms between 400 and 700°C • Nanocrystalline high-temperature

		• 2400 nm FeOH band disappears by 400-600°C	phases formed between 700° and 1000° C. • Air versus CO_2 results similar above 1100 nm
Morris et al. (2010)	• <38 µm and <150 µm nontronite powders (2 different samples) • 350-2500 nm wavelength range • Stepwise heating to 50°, 105°, and 210°C for variable lengths of time • Ambient pressure, purged with dry N2. • Samples also analyzed by XRD and Mossbauer spectroscopy	• spectra become darker and redder with increasing temperature, • Fe^{3+} bands below ~1000 nm broaden, bands disappear between 105 and 210°C. • 650 nm band and 750 nm maximum become indistinct at 105°C • Loss of 1400 and 1900 nm hydration bands at 210°C • 2230 and 2400 nm FeOH bands persist to 210°C	• Interlayer water lost above ~210°C; smectite structure retained • No Fe^{2+} produced
Che and Glotch (2012)	• <2 µm nontronite powders (2 samples), pressed into pellets • 1200-2500 nm and 7.1-100 µm wavelength ranges • Stepwise heating: 24 hours each to 100, 200, 300, 400, 500, 600, 700, 800, and 900°C. • Ambient terrestrial atmospheric pressure, purged to remove CO_2 and water vapor for spectral measurements. • Samples also analyzed by differential scanning calorimetry	• Loss of 1400 nm band by 400° C. • 1400 nm hydration band disappears between 300 and 400°C • 1900 nm hydration band lost between 600 and 700°C • 2280 and 2400 nm FeOH bands largely unchanged to 300°C, weaken and disappear by 700°C.	• Shapes, minima and maxima in DSC traces vary for different nontronite samples. • DSC endotherm at 109 or 134°C • No new spectral bands produced with increasing temperature
Gavin et al. (2013)	• Shock experiments; 2.07-3.27 km/s projectile velocities; corresponding to 80-137° C average temperatures, 220-524° C peak temperatures, 0.9-1.6 GPa average pressures, and 5.4-17.5 GPa peak pressures • <63 µm nontronite powder • 1000-2500 nm and 1.4-28.6 µm wavelength ranges • Shock experiments conducted in	• 1400 and 1900 nm hydration bands increase slightly in depth • New band seen at 2100 nm • 2280 and 2400 nm FeOH bands unchanged. • No color change observed.	• Sample underwent partial structural deformation or amorphization • Mid-infrared spectral changes greater than vis-NIR spectral changes

	ambient air. • Samples heated to 150°C in dry N_2 prior to spectral measurements • Samples also analyzed by XRD, Raman spectroscopy, and cathodoluminescence.		
Friedlander et al. (2015)	• Shock experiments; 0.9-1.3 km/s projectile velocities; corresponding to 10.2-39.1 GPa peak pressures • <2 µm nontronite powder, pressed into pellets • 350-2500 nm and 2.5-50 µm wavelength range • Samples also analyzed by Raman, TEM, XRD, and Mossbauer spectroscopy	• 650 nm band largely disappears by 10.2 GPa; spectra become redder up to 34.6 GPa • 750 nm local maximum present to maximum shock pressure • Below ~1000 nm, Fe^{3+}-associated absorption bands become broader and merge above 19.7 GPa • 1400 and 1900 nm hydration bands present to maximum pressure (39.1 GPa), but weaken • 2165 and 2210 nm AlOH bands disappears at 25.2 GPa and re-emerges as a single band at 34.6 GPa • 2280 nm FeOH band shifts to shorter wavelengths; 2400 nm FeOH band shifts to longer wavelengths and both disappears by 34.6 GPa	• Samples can become structurally deformed and partially dehydroxylated. • Fe^{3+} site becomes distorted and partial OH group loss • Highest shock pressure results in largely amorphous material
Michalski et al. (2017)	• Shock experiments; in air; ~10-40 GPa peak pressures • <2 µm nontronite powder, pressed into pellets (70 MPa pressure) • 350-2500 nm wavelength range • Samples also analyzed by TEM, XRD, and Mossbauer spectroscopy	• 1400 and 1900 nm hydration bands present to maximum pressure (40 GPa), but generally weaken • 2165 and 2210 nm AlOH bands disappear between 10 and 20 GPa and re-emerge as a single band at higher shock pressures	

		• 2290 nm FeOH band lost between 10 and 20 GPa; 2400 nm FeOH band lost by ~10 GPa	
This study	• <45 µm nontronite powder (NON101) • 350-2500 nm wavelength range • 5 Torr (660 Pa) CO_2 for 7 days • Sample analyzed by XRD, XRF, and wet chemistry	• <1000 nm Fe^{3+} bands persist; largely unchanged • Reduction in 1400 and 1900 nm hydration band depths • ~2280 and 2400 nm FeOH bands unaffected	
This study	• <45 µm nontronite powders (NON101-NON105) • Multiple grain sizes of NON105 • 350-2500 nm wavelength range	• Grain size increase reduces overall reflectance • No measurable differences in Fe^{3+}-associated absorption bands below 1000 nm • No variation in position of 2280 and 2400 nm FeOH bands	
This study	• <45 µm nontronite powders (NON101) • 350-2500 nm wavelength range • 1 week each at 110°, 130°C, and 300°C in ~40 Torr (660 Pa) CO_2 • Sample analyzed by XRD, XRF and wet chemistry	• 650 nm Fe^{3+}-associated band and local maximum near 750 nm disappear by 110°C • Spectrum below ~1400 nm becomes flatter • Spectra above 1400 nm generally become redder • Reduction in 1400 and 1900 nm hydration band depths • ~2280 and 2400 nm FeOH bands persist but become shallower • Hematite-like spectral features start to appear between 180 and 300°C; i.e., steeper slope below 700 nm and absorption band near 830 nm	

Highlights:

- A suite of nontronite samples was characterized compositionally, structurally, and by reflectance spectroscopy
- Nontronite reflectance spectra are characterized by several diagnostic Fe-OH absorption bands, particularly in the 2280 and ~2400 nm regions
- The 2280 nm absorption feature and the absence of a strong ~2320 nm absorption band are unique to nontronites
- Heating up to 300°C in a Mars-like atmosphere demonstrates the spectral robustness of the ~2280-2290 nm absorption feature